
Article:
Doyle, Scott James, Gibson, Andrew Robert orcid.org/0000-0002-1082-4359, Boswell, Rod et al. (2 more authors) (2019) Control of electron, ion and neutral heating in a radio-frequency electrothermal microthruster via dual-frequency voltage waveforms. Plasma Sources Science and Technology. 035019. ISSN 0963-0252

https://doi.org/10.1088/1361-6595/ab0984

Control of electron, ion and neutral heating in a radio-frequency electrothermal microthruster via dual-frequency voltage waveforms

Control of electron, ion and neutral heating in a radio-frequency electrothermal microthruster via dual-frequency voltage waveforms

Scott J. Doyle[1], Andrew R. Gibson[1,2], Rod W. Boswell[3], Christine Charles[3], and James P. Dedrick[1]

[1]York Plasma Institute, Department of Physics, University of York, Heslington, York, YO10 5DD, UK

[2]Institute of Electrical Engineering and Plasma Technology, Ruhr-Universität Bochum, Universitätsstraße 150, 44801 Bochum, Germany

[3]Space Plasma, Power and Propulsion Laboratory, Research School of Physics and Engineering, The Australian National University, ACT 0200, Australia

E-mail: sjd549@york.ac.uk

January 15, 2019

Abstract

The development of low power micro-propulsion sources is of recent interest for application on miniature satellite platforms. Radio-frequency (rf) plasma electrothermal microthrusters can operate without a space-charge neutralizer and provide increased control of spatiotemporal power deposition. Further understanding of how the phase-resolved rf plasma heating mechanisms affect the phase-averaged bulk plasma properties, e.g. neutral gas temperature, could allow for in-flight tailoring of plasma thrusters. In this work, experimentally validated two-dimensional fluid-kinetic simulations were employed to study the spatially resolved electron and ion power deposition and neutral gas heating in a dual-frequency rf electrothermal microthruster operating at 1.5 Torr plenum pressure in argon. Experimental validation was performed through a comparison of the measured and simulated phase resolved Ar($2p_1$) excitation rates, showing close agreement. Two types of dual-frequency voltage waveforms were investigated, and comprise the combination of a 13.56 MHz voltage waveform with 27.12 MHz and 40.68 MHz waveforms, respectively. Varying the phase offset of the higher harmonic relative to the fundamental 13.56 MHz voltage waveform was found to modulate the dc self-bias voltage by 11% and 3% of the maximum applied peak-to-peak voltage, respectively. The 13.56 MHz, 27.12 MHz dual-frequency voltage waveform provided the highest

degree of control, where the fraction of total rf power deposited into Ar^+ ions was found to vary from 57% to 77%, modulating the on-axis neutral gas temperature by 35%. This control is attributed to the variation in the fraction of the rf phase cycle for which the sheath is collapsed, altering the phase-averaged electric field strength adjacent to the radial wall. The application of dual-frequency waveforms provides the ability to optimize the particle heating mechanisms with application to electrothermal propulsion.

1 Introduction

Electric propulsion (EP) sources are an established alternative to traditional cold-gas and monopropellant thrusters for employment on satellites[1,2]. The miniaturization of EP sources for micro-satellites is an increasingly important area of research, resulting in the development of new compact, low-power and charge-neutral[3], prototypes[4–6]. Electrothermal EP sources are particularly suited to miniaturization as the maximum gas temperature typically scales inversely with the thruster volume[1].

One such electrothermal thruster is the Pocket Rocket, a low power ($\leq$ 50 W) asymmetric radio-frequency (rf) capacitively coupled micro-thruster[7–13]. The Pocket Rocket operates at a relatively high pressure ($\geq$ 133 Pa (1 Torr)) as this represents the Paschen (pressure $\times$ distance) minimum for ignition for the dimensions of the source[14]. The thruster is typically powered by a 12.8 - 13.8 MHz rf voltage[15], where power is deposited into the propellant primarily through ion-neutral charge exchange collisions in the powered electrode sheath[9,16]. Thrust is produced as the hot (1000 K) neutrals exit the thruster in an exhaust plume. As the exhaust is neutral no external neutralizer is required[17]. The thruster and power supply have recently been demonstrated to fit within a standard 1U CubeSat frame, as described in Ref. 2 and 15.

The physically asymmetric geometry of the Pocket Rocket thruster ensures that a substantial negative dc self-bias voltage forms on the radial dielectric wall adjacent to the powered electrode[9]. This dc self-bias voltage forms to balance the net positive and negative fluxes onto the radial wall[18]. Altering this dc self-bias voltage will vary the radial ion flux onto the thruster walls, and consequentially the resulting neutral gas temperature through a regulation of ion-neutral charge exchange collision frequency[19,20].

Control of the dc self-bias voltage, and hence the bulk properties, in capacitively coupled rf plasmas can be achieved through the application of multiple harmonics with varying phase offsets to produce distinct rf waveforms that exhibit either amplitude or slope asymmetries[21–24]. By applying two or more harmonics of the same amplitude and by varying the phase offset of the higher harmonic it is possible to introduce a phase-averaged electrical asymmetry to the plasma[18,25]. This electrical asymmetry effect (EAE) can also modify any existing physical or secondary electron induced asymmetries[26–28]. This provides a mechanism whereby the dc self-bias voltage can be controlled in real-time for a given plasma source configuration, as the relative phase offset between any two harmonics can be readily changed[22,29,30]. Control of the sheath voltage is also possible without the EAE using electrically symmetric dual-frequency waveforms, consisting of a first and third harmonic (13.56 MHz and 40.68 MHz)[31,32]. The use of 'tailored' and dual-frequency voltage waveforms in planar capacitively coupled rf plasmas is already established[23,33–37]. However, recent work has begun to focus application

in non-planar geometries[30,38], more closely matching the physically asymmetric conditions found in many technological reactors.

Capacitively coupled plasmas exhibit a number of different electron and neutral gas heating mechanisms. Ion-neutral charge exchange collisions have already been introduced as the primary neutral gas heating mechanism in the Pocket Rocket[9,11], however a number of electron heating mechanisms are also present. For example, there exists substantial electron heating during phases of sheath expansion and contraction (maximum $\mathrm{d}V/\mathrm{d}t$) due to the high electron fluxes near the moving sheath edge[16,29,39,40]. As the ion flux onto material surfaces becomes significant through either increased applied voltage or increased dc self-bias voltage, the emission of high energy secondary electrons from material surfaces also becomes important[41]. As these secondary electrons are accelerated back into the plasma through the sheath potential, they reach their highest energy ($\geq$ 50 eV) at phases of maximum sheath width and are capable of playing an important role in plasma sustainment[42,43].

The electron heating mechanisms in the Pocket Rocket primarily arise in response to the phase-resolved sheath dynamics, e.g. sheath expansion and collapse heating and γ-mode heating from secondary electron collisions[16]. Altering the shape of the applied voltage waveform affects these mechanisms directly as the phase-resolved sheath width mirrors the applied voltage amplitude[33,44,45]. In the case of dual-frequency waveforms, the waveform shape can be changed through varying the phase offset between each harmonic. The altered waveform shape varies the electrical symmetry, providing a control mechanism for the EAE and, in turn, provides control over the phase-resolved electron heating mechanisms via the sheath dynamics and the phase-averaged neutral gas heating via the dc self-bias voltage.

In this work, two dimensional fluid-kinetic simulations of a dual-frequency driven rf microthruster were performed, where the dual-frequency voltage waveforms comprised a fundamental 13.56 MHz waveform combined with a 27.12 MHz or 40.68 MHz waveform with a variable phase offset. A description of the simulation geometry and operating parameters is given in section 2, and the simulation theory and dual-frequency model are discussed in sections 2.1 and 2.2, respectively. The experimental setup and method are briefly discussed in section 3. The effects of varying phase offset on the spatial rf-power deposition and fraction of power deposited into Ar^+ ions and electrons are presented in sections 4.1 and 4.2, respectively. A discussion of the spatio-temporal electron heating mechanisms with respect to the sheath dynamics is presented in sections 5.1 and 5.2. To validate these electron heating dynamics predicted by the simulations, a comparison between measured and simulated excitation rates into the Ar(2p1) state is presented in section 5.3. Finally, the trends in the Ar^+ ion energy distribution functions (IEDFs) incident on the radial wall with varying applied phase offset are

presented in section 5.4.

2 Description of the simulation model

Two-dimensional, fluid-kinetic simulations were undertaken using the Hybrid Plasma Equipment Model (HPEM)[46]. The HPEM model has previously been corroborated with phase-resolved optical emission spectroscopy (PROES)[47–49] measurements of the Pocket Rocket in Ref. 16.

The Pocket Rocket mesh geometry is illustrated in figure 1. An external circuit (not shown) comprising of an rf voltage source and blocking capacitor is connected to the powered electrode. Although a blocking capacitor is included within the circuit, the alumina dielectric layer prevents a dc current back to the power source and maintains the phase-averaged dc self-bias voltage as a negative surface charge.

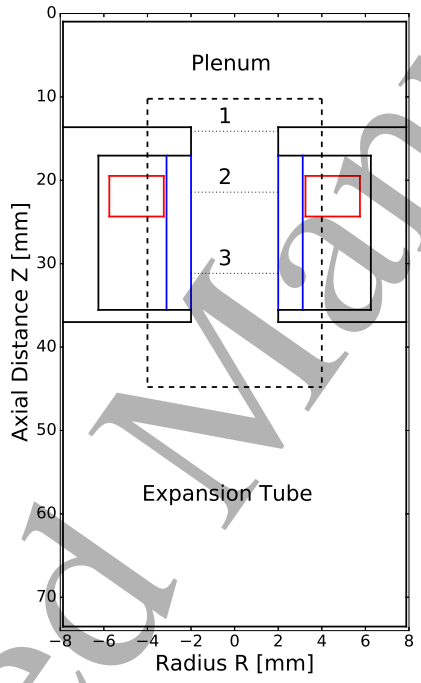

Figure 1: Illustration of the simulation domain (not to scale), the domain is radially symmetric around R = 0.0 mm. Gas is introduced into the plenum and extracted at the end of the expansion tube. An rf voltage is applied to the electrode, denoted in red, and couples to the plasma through an alumina tube, denoted in blue. The source region, highlighted by dashed lines, contains three sub-regions of interest, denoted by dotted lines: upstream (Z = 14.2 mm), powered electrode (Z = 21 mm) and downstream (Z = 31 mm), regions 1, 2 and 3, respectively.

The source is operated in argon with an input flowrate of 100 sccm and a pressure of 113 Pa (0.85 Torr) at the outlet of the expansion tube (Z = 73 mm), resulting in a plenum pressure of 200 Pa (1.5 Torr), closely matching experimental conditions[16]. The powered electrode is driven by a 600 V_{pp} dual-frequency 13.56 MHz, 27.12 MHz or 13.56 MHz, 40.68 MHz voltage waveform. The mesh consists of 64 × 152 (R × Z) cells in a cylindrically symmetric geometry, corresponding to a radial resolution of 0.125 mm per cell and an axial resolution of 0.5 mm per cell. The higher radial resolution is required

to resolve the radial electric field gradient through the powered electrode sheaths and determine the sheath thickness and velocity.

Three regions of interest are identified in figure 1: region 1 (Z = 14.2 mm), upstream of the powered electrode, region 2 (Z = 21 mm), on-axis adjacent to the powered electrode and region 3 (Z = 31 mm), downstream of the powered electrode. IEDFs presented in section 5.4 are obtained from the alumina surface adjacent to the powered electrode in region 2, Z = 21 mm, R = 2.1 mm.

2.1 Simulation theory

Simulations were performed under the same conditions as previous work in Ref. 16, as such, only a brief overview is presented.

The particle species included in the simulation are: Ar, Ar($1s_2$), Ar($1s_3$), Ar($1s_4$), Ar($1s_5$), Ar($4p$), Ar($4d$), Ar_2^*, Ar^+, Ar_2^+ and e^-, where the reaction mechanism is as discussed in Ref. 50. Two classes of electrons are considered, those produced during ionizations within the plasma and those released from material surfaces (secondary electrons). The time and space resolved energy distribution functions of electrons produced in the gas-phase are obtained from the solution of the two-term Boltzmann equation. The energy distribution functions of all heavy particle species are assumed to be Maxwellian and the distribution function of secondary electrons are obtained via a Monte Carlo algorithm. Secondary electrons are released from material surfaces in proportion to the ion fluxes incident on that surface and its energy independent secondary electron emission coefficient[51,52]. Secondary electron emission coefficients are set to $\gamma = 0.2$ and $\gamma = 0.0$ at the surface of the alumina wall and outside of the plasma source, respectively.

Electron-neutral and electron-ion collisions solved for in the model include elastic, excitation and ionization reactions. As described in Ref. 50, cascade processes, multi-step ionization and heavy particle mixing between excited species are also included, the interaction cross-sections for which are obtained from Refs. 53–57. Ion-neutral charge exchange collisions are employed with a rate coefficient of 5.66×10^{-10} cm^{-3} $(T_g/300)^{0.5}$ where T_g is the neutral-gas temperature[58]. Ions that do not undergo charge-exchange collisions will collide with the radial wall, depositing their kinetic energy and remaining potential energy following Auger recombination. Conductive heat diffusion is applied at plasma-material interfaces with a thermal energy accommodation coefficient of 0.4 with all material surfaces initiated to 325 K unless otherwise stated. Further discussion on the choice of thermal energy accommodation coefficient and its role are given in Refs. 59 and 16

The ion energy distributions for Ar^+ incident on the radial wall are obtained via a Monte-Carlo algorithm[46]. In this case, Ar^+ psuedoparticles are released stochastically from cells throughout the

plasma volume. Psuedoparticles are treated kinetically, subject to local electrostatic forces, until they undergo a collision or impact onto a material surface. Collision probabilities are derived from the same reaction mechanism as used in the gas-phase.

Simulated phase-resolved optical emission spectroscopy (PROES)[48,60] images, presented in section 5, were generated using the same technique as described in Ref. 16. A depth of field of 24 mm was applied to the simulated PROES images, such that ionization from the full length of the source tube (Z = 13 mm - 37 mm) is taken into account, more closely approximating measured images, discussed in section 3.

2.2 Dual-frequency voltage waveforms

Dual-frequency voltage waveforms, constructed through the superposition of a fundamental 13.56 MHz sinusoid and either a 27.12 MHz or 40.68 MHz sinusoid with a variable phase offset, were generated using equation 1:

$$\phi_{\mathrm{rf}}(t) = \sum_{k=1}^{n} \left(\frac{\phi_0}{n}\right) \sin(k\omega_0 \mathrm{t} + \theta_k) \tag{1}$$

where $\phi_{\mathrm{rf}}(t)$ is the time dependent voltage of the combined waveform, ϕ_0 is its maximum amplitude, $\omega_0 = 2\pi f_0$ is the fundamental angular frequency, θ_k is the phase offset of harmonic k and n is the total number of applied harmonics. When evaluating $\phi_{\mathrm{rf}}(t)$, $k = 1{,}2$ for 'odd-even' voltage waveforms that comprise 13.56 MHz and 27.12 MHz components or $k = 1{,}3$ for 'odd-odd' voltage waveforms comprising 13.56 MHz and 40.68 MHz components. Phase offsets are applied only to the higher harmonic such that $\theta_1 = 0°$ and $0° < \theta_{2,3} < 360°$. From this point forward phase offsets θ_2 and θ_3 are referred to as θ for simplicity.

As the harmonics $k = 2$ (27.12 MHz) and $k = 3$ (40.68 MHz) do not add in phase with the fundamental 13.56 MHz harmonic, the peak-to-peak voltage $\mathrm{V_{pp}}$ of the combined dual-frequency voltage waveform, described by $\phi_{\mathrm{rf}}(t)$, depends upon θ. Arising from this, the positive amplitude, $\phi^{+}_{\mathrm{rf}}(t)$, and negative amplitude, $\phi^{-}_{\mathrm{rf}}(t)$, are not always equal. Hence the dual-frequency voltage waveforms do not have a single voltage amplitude. For ease of discussion, waveforms will be discussed in terms of their peak-to-peak voltage:

$$V_{\mathrm{pp}} = |\max \phi_{\mathrm{rf}}(t)| + |\min \phi_{\mathrm{rf}}(t)| \tag{2}$$

In this study, the $\mathrm{V_{pp}}$ for each dual-frequency voltage waveform was allowed to vary with phase offset to more closely match experimental conditions. The variation in $\mathrm{V_{pp}}$ for odd-even and odd-odd

dual-frequency voltage waveforms generated using equation 1 with varying phase offset θ is shown in figure 2.

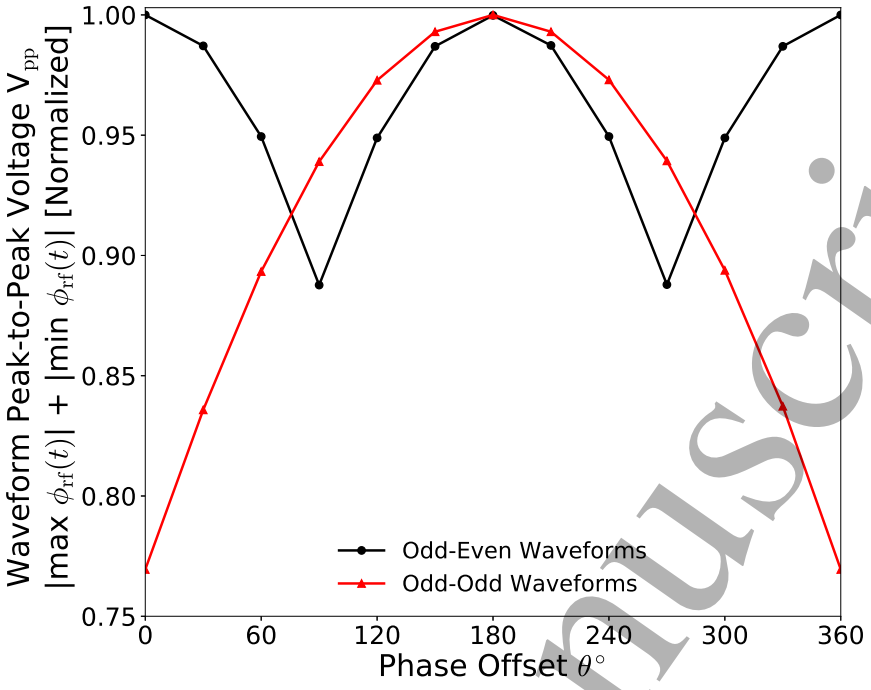

Figure 2: Peak-to-peak voltages V_{pp} for dual-frequency voltage waveforms generated using equation 1 for (a) odd-even ($k = 1, 2$) and (b) odd-odd ($k = 1, 3$) configurations with phase offsets $0° \leq \theta \leq 360°$ and $\phi_0 = 600$ V. Odd-even and odd-odd peak-to-peak voltages are normalised to their respective maximum; odd-even: 528 V, odd-odd: 600 V.

As shown in figure 2, the relationship between V_{pp} and the applied phase offset differs for odd-odd and odd-even waveforms. For odd-even waveforms ($k = 1, 2$), there is a periodic reduction in the peak-to-peak voltage for every 180° phase offset. Over a 360° range of phase offsets, two maxima and minima in V_{pp} occur, separated by 90°, where the difference between maximum and minimum represents 11% of the maximum odd-even V_{pp} (528 V at $\theta = 0°$, $\theta = 180°$, $\theta = 360°$). Conversely, in figure 2 a single approximately parabolic variation in V_{pp} is observed over the 360° range of phase offsets for odd-odd waveforms ($k = 1, 3$). Maxima and minima are separated by 180° of phase offset, double that of the odd-even waveforms, while the variation between these increases to 26% of the maximum V_{pp} (600 V at $\theta = 180°$).

Examples of simulated dual-frequency voltage waveforms for three phase offsets ($\theta = 0°, \theta = 45°, \theta = 90°$) generated using equation 1 with odd-even ($k = 1, 2$) and odd-odd ($k = 1, 3$) voltage waveform components are shown in figures 3 (a) and (b), respectively.

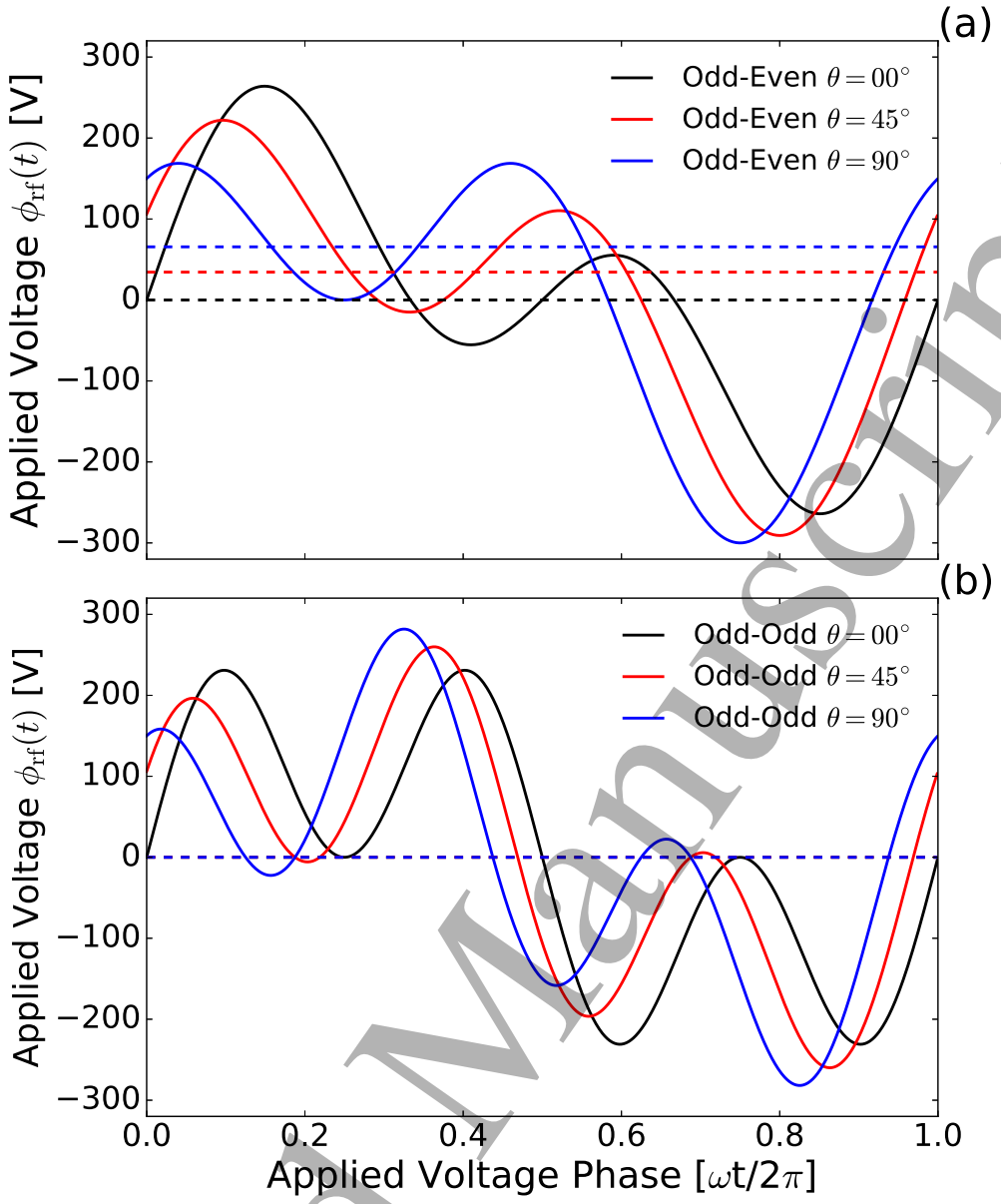

Figure 3: Dual-frequency voltage waveforms generated using equation 1 for (a) odd-even ($k = 1, 2$) and (b) odd-odd ($k = 1, 3$) configurations with phase offsets $\theta = 0°, \theta = 45°, \theta = 90°$, with $\phi_0 = 600$ V. The difference between the most negative and most positive voltages for each waveform are denoted by the dashed lines, noting that this difference is zero in the case of odd-odd waveforms in (b).

Here, the phase offset θ refers to the temporal delay between the two superimposed waveforms, while applied voltage phase $\tau = \omega t/2\pi$ refers to temporal position within the rf cycle. Varying the phase offset of an even (k=2) harmonic relative to the fundamental frequency alters the phase-averaged voltage ($V_{\rm pp}/2$) of the resulting waveform $\phi_{\rm rf}(t)$. This is demonstrated for three odd-even waveforms in figure 3 (a), where the phase of the 27.12 MHz harmonic is offset from the fundamental harmonic by $\theta = 0°$, $\theta = 45°$ and $\theta = 90°$. Varying the phase offset causes the extrema in amplitude of the k=1 and k=2 harmonics to add asymmetrically, where the variation in positive amplitude need not match the variation in the negative amplitude, i.e. $\phi^{+}_{\rm rf}(t) - \phi^{-}_{\rm rf}(t) \neq 0$. This results in a non-zero phase-averaged voltage, denoted by the dotted lines, and is referred to as the electrical asymmetry

effect (EAE)[21,24].

The same effect is not observed for an odd-odd waveform, where the same phase offsets are applied to the odd (k=3) 40.68 MHz harmonic, shown in 3 (b). Applying a phase offset to an odd-odd waveform results in the extrema of the k=1 and k=3 harmonics superimposing symmetrically. This ensures that the extrema of the positive and negative voltages are equal, i.e. $\phi^{+}_{\mathrm{rf}}(t) - \phi^{-}_{\mathrm{rf}}(t) = 0$ and therefore no electrical asymmetry is present. Although this symmetry in the voltage amplitudes negates any electrical asymmetry, the peak-to-peak voltage, V_{pp}, defined in equation 2, is not independent of phase offset. The location and magnitude of the peak change in voltage is also affected, altering the phase-resolved sheath dynamics.

The sheath width varies as a function of the axial distance Z and rf voltage phase τ. The sheath edge $S(\mathrm{Z},\tau)$ was determined as the radius R satisfying the Brinkmann criterion[61]:

$$\int_{0}^{S(\mathrm{Z},\tau)} n_e(R,\tau)\mathrm{d}R = \int_{S(\mathrm{Z},\tau)}^{L/2} n_{\mathrm{eff}}(R,\tau) - n_e(R,\tau)\mathrm{d}R \tag{3}$$

where, $L/2$ represents the centre of the plasma bulk, defined as the radius of most positive plasma potential and is typically R = 0.0 mm for the Pocket Rocket geometry. The effective positive charge density is denoted n_{eff} where $n_{\mathrm{eff}} = n_{\mathrm{Ar}^{+}}$ in this case, and n_e is the electron density. In practice, the Ar^{+} density is integrated radially from the radial wall towards $L/2$, while the electron density is integrated from $L/2$ towards the radial wall. The radius for which equation 3 is true is taken as the sheath edge. As the radius is defined as zero on-axis, see figure 1, the sheath width is defined as: $S_{\mathrm{x}} = 2.1 - S(\mathrm{Z},\tau)$ mm, where the source radius is 2.1 mm.

3 Experimental Setup

The Pocket Rocket source, power coupling circuit and optical measurement configuration have been described in detail previously in Ref 16, and so are only briefly outlined here. The Pocket Rocket source and associated power circuit is illustrated in figure 4.

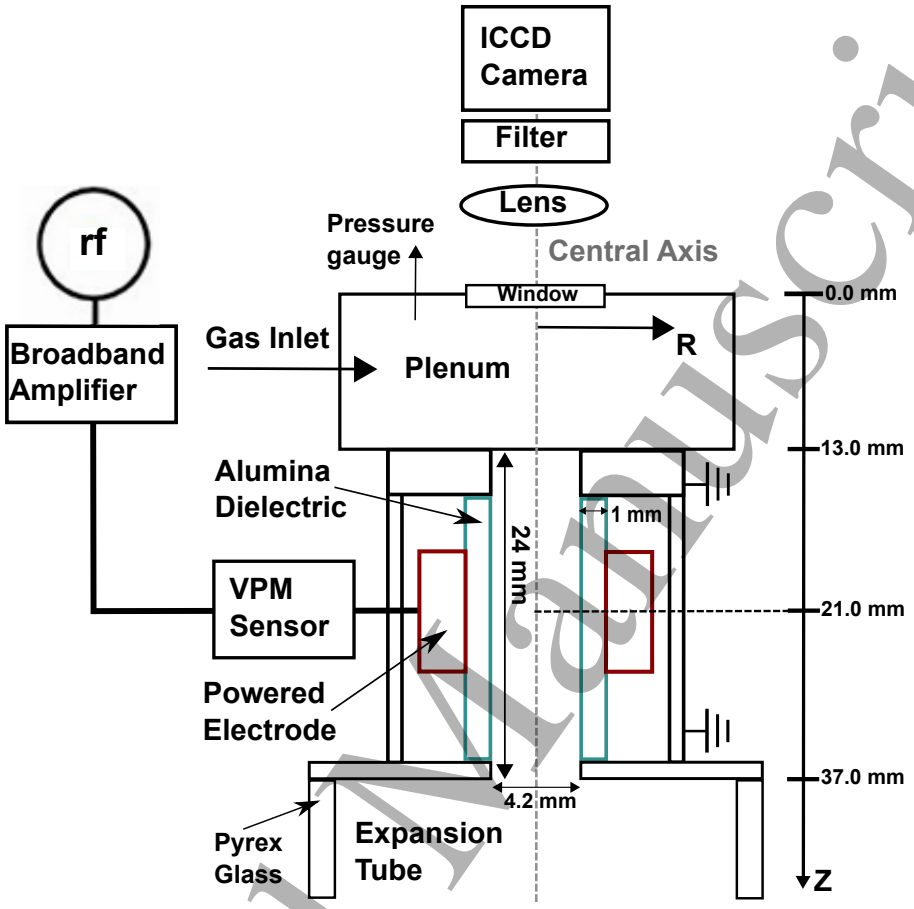

Figure 4: Schematic of the experimental setup (not to scale), showing the power coupling circuit and the orientation of the camera with respect to the plasma source[16].

The source was operated with a dual-frequency 13.56 MHz and 27.12 MHz voltage waveform, constructed as described by equation 1, and supplied via an arbitrary waveform generator (Keysight 33621A, 120 MHz), and a broadband amplifier (IFI SCCX100, 0.01 - 220 MHz), shown in figure 4. The source was operated in argon, maintaining a plenum pressure of 207 Pa (1.55 Torr) during a steady-state discharge. Images were recorded by an ICCD camera (Andor iStar DH344T-18U-73 1024 $\times$ 1024 array, pixel size 13 $\times$ 13 μm^2, employing a 750.446 nm bandpass filter (LOT-QuantumDesign, 1 nm FWHM). The depth of field exceeds the axial dimension of the source and was taken to be 24 mm for the purposes of analysis.

PROES images were obtained as the optical emission from Ar($2p_1$) - Ar($1s_2$) at 750.4 nm, measured in phase with the 13.56 MHz fundamental voltage frequency. The phase resolved optical emission was post-processed to extract the electron impact excitation rate of the Ar(2p1) state by assuming

depopulation of the state through spontaneous emission and collisional quenching only. A neutral argon quenching coefficient of $k_{Ar} = 1.6 \times 10^{-17}$ $\mathrm{m^3 s^{-1}}$ was employed, representing a neutral gas temperature of 1000 K[60,62].

4 Varying phase offset - effects on plasma power deposition

The dc self-bias voltage η, normalized to V_{pp}, present on the alumina radial wall adjacent to the powered electrode (region 2, Z = 21 mm) is shown with respect to phase offset for odd-even and odd-odd waveforms in figure 5 (a). The total rf power deposited is shown in figure 5 (b) and the maximum secondary electron ionization rate and radial Ar^+ flux at the powered electrode, (region 2, Z = 21 mm), are shown in figures 5 (c) and (d), respectively.

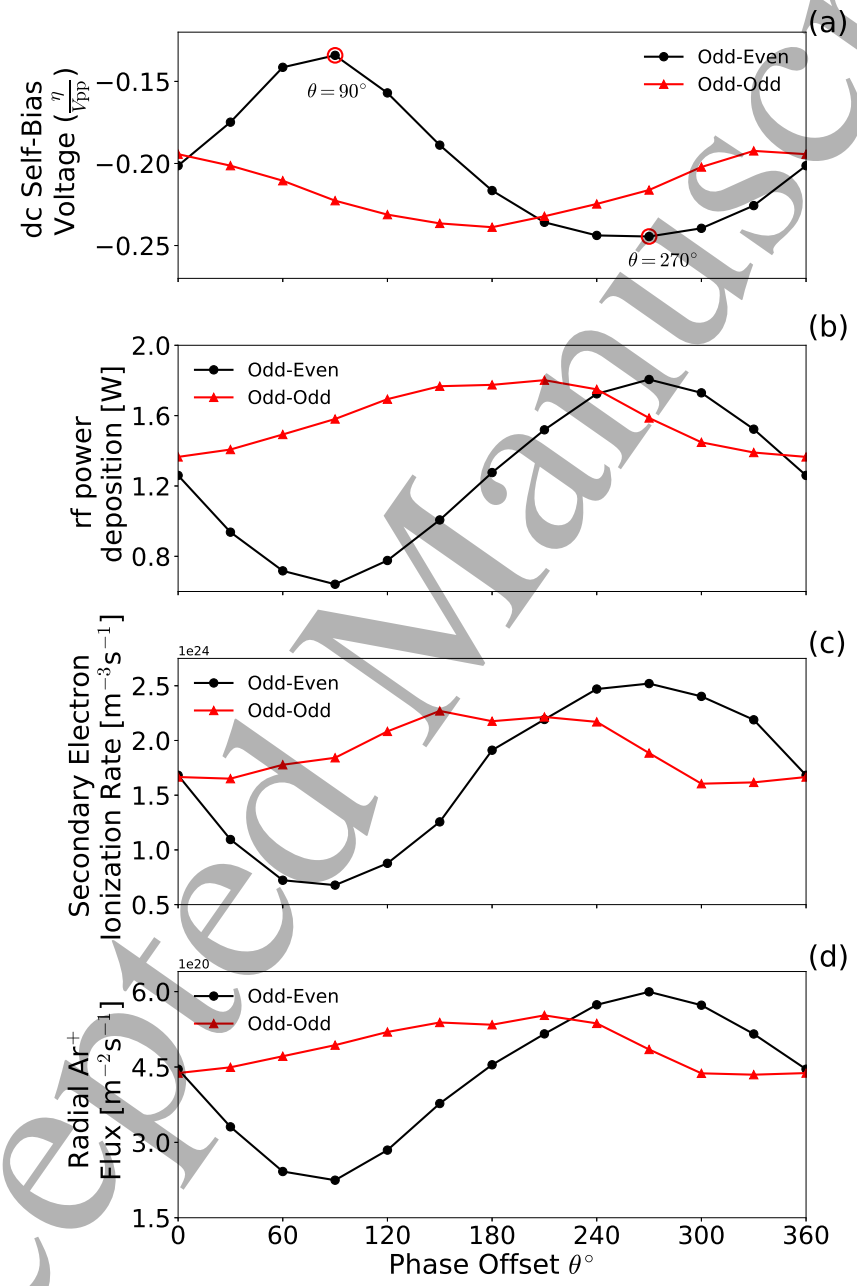

Figure 5: Phase-averaged (a) dc self-bias voltage adjacent to the powered electrode (R = 2.1 mm), (b) total rf power deposition, (c) secondary electron ionisation rate and (d) radial Ar^+ flux with respect to phase offset θ for odd-even and odd-odd voltage waveforms. Radial Ar^+ flux and secondary electron impact ionisation rates are taken at the dielectric surface adjacent to the powered electrode (R,Z = 2.1 mm, 21 mm). The phase offsets which correspond to the most positive and most negative dc self-bias voltages are identified with red circles in (a). Plenum pressure 200 Pa (1.5 Torr), ϕ_0 = 600 V.

Varying the phase offset in the odd-even waveform applied an electrical asymmetry to the plasma. This resulted in an approximately sinusoidal modulation of the dc self-bias voltage in figure 5 (a) as the phase offset was varied through $0° \leq \theta \leq 360°$. The dc self-bias voltage was modulated by 11% V_{pp} and 3% V_{pp} for the odd-even and odd-odd voltage waveforms, respectively. The dc self-bias did not vary about zero due to the inherent physical asymmetry arising from the smaller powered electrode area as compared to the larger combined grounded electrode areas.

The most negative dc self-bias voltages for the odd-even and odd-odd voltage waveforms occurred at $\theta = 270°$ and $\theta = 180°$ phase offsets, respectively. These phase offsets resulted in the highest secondary electron ionization rates, as shown in figure 5 (c), and hence the highest plasma densities. The variation in secondary electron ionization rate resulted in a 225% variation in the Ar^+ density between $90° \leq \theta \leq 270°$ using odd-even applied voltage waveforms. Note that these phase offsets represent the minima in the odd-even waveform peak-to-peak voltage as shown in figure 2.

Despite the odd-odd waveform having applied no direct electrical asymmetry to the plasma, there was still a non-zero modulation in the dc self-bias voltage, 5 (a). The mechanism for this modulation is attributed to the variation in the peak-to-peak voltage (2) and associated variation in the power deposited with phase offset, see figure 5 (b). The increased rf-power deposition in figure 5 (b) coincides with an increased ionization rate adjacent to the powered electrode in figure 5 (c). The increased ionization rate leads to a corresponding increase in plasma density adjacent to the powered electrode, which reduces the phase-averaged sheath width, increasing the sheath capacitance, and results in a larger negative charge being held on the alumina surface[18]. The increased Ar^+ density also increases the electrical conductivity close to the powered electrode, increasing the power deposited for a given applied voltage. The same mechanisms are observed in single frequency parallel plate discharges where the dc self-bias voltage increases with increasing applied voltage[20].

Odd-even waveforms provide a much greater control over the secondary electron ionization rate in figure 5 (c) due to the direct application of an electrical asymmetry, observed in figure 5 (a). As the dc self-bias voltage becomes more negative, the radial Ar^+ ion flux incident on the radial wall increases as shown in figure 5 (d). This is in-fact the purpose of the dc self-bias voltage formation, to balance the charges leaving the plasma[18]. The radial flux in figure 5 (d) was modulated by a factor of 3 over the range $90° \leq \theta \leq 270°$ for odd-even waveform operation. As the plasma density was only modulated by a factor of 2 over the same range of phase offsets, and flux is the density velocity product, the radial velocity of the ions increases to account for the larger flux modulation.

4.1 Spatial power deposition

The phase-averaged spatial distribution of the rf power deposited into the plasma and resulting neutral gas temperatures for odd-even voltage waveforms are shown in figure 6. Odd-even voltage waveforms were chosen as they provided a greater degree of control than the odd-odd waveforms, allowing for an easier observation of trends. Here, panels (a) and (c) show the most positive dc self-bias voltage ($\theta = 90°$), while panels (b) and (d) show the most negative dc self-bias voltage ($\theta = 270°$), respectively, representing the highlighted data points shown previously in figure 5 (a).

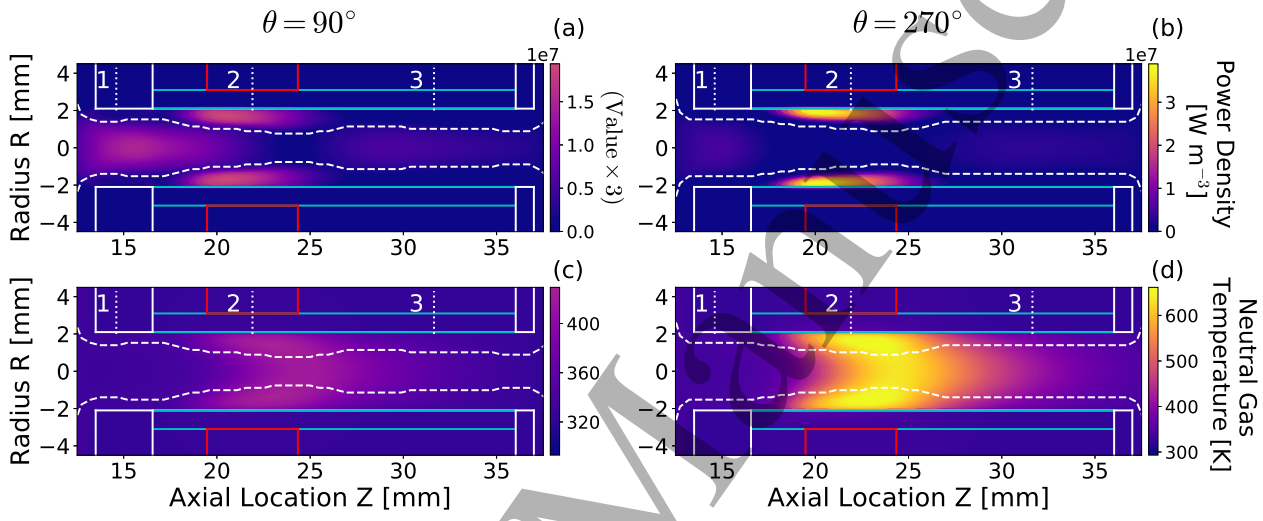

Figure 6: Phase-averaged (a), (b) rf power density and (c), (d) neutral gas temperature for 90° and 270° phase offsets, representing most positive and negative dc self-bias voltages, respectively. The dashed white lines represent the phase-averaged sheath edge. Plenum pressure 200 Pa (1.5 Torr), odd-even voltage waveforms, $\phi_0 = 600$ V. Panel (a) has been scaled by a factor of three for clarity.

The spatial power deposition varied substantially between figures 6 (a) and (b), where the proportion of power deposited on-axis decreased as the phase offset was increased from 90° to 270°, i.e. as the dc self-bias voltage becomes more negative. The on-axis power deposition in figure 6 (a) is consistent with an α-mode discharge where power is primarily deposited through sheath movement and electron collisions in the bulk plasma, while figure 6 (b) is more representative of γ-mode operation where the plasma is primarily sustained through ionization by secondary electrons[10,16,63,64].

As the phase offset was varied through $90° \leq \theta \leq 270°$ the total rf power deposited into the plasma increased by 140%, from 0.35 W to 0.83 W. However, the power deposited into electrons only increased by 31%, from 0.19 W to 0.25 W. It follows that a larger fraction of the total power was deposited into Ar^+ ions at the most negative dc self-bias voltage ($\theta = 270°$), as compared to the most positive

($\theta = 90°$). Specifically, the fraction of the total rf-power deposited into ions increased from 57% to 77% between the extrema in dc self-bias voltages.

The neutral gas temperature increased in proportion to the rf power deposited, shown in figures 6 (c) and (d) for $\theta = 90°$ and $\theta = 270°$, corresponding to minimum and maximum dc self-bias voltages, respectively. The maximum on-axis neutral gas temperature at region 2 (R,Z = 0 mm, 21 mm) adjacent to the powered electrode sheath increased from 424 K to 652 K, varying by 35% through $90° \leq \theta \leq 270°$. Despite this variation in the value of the neutral gas temperature, the location of maximum temperature was approximately independent of the phase offset. Neutral gas heating was predominately located within the powered electrode sheath, with a radial diffusion towards the central axis of the thruster (R = 0.0 mm). Power deposited on-axis upstream of the powered electrode (region 1) in figure 6 (a) does not contribute significantly to the neutral gas heating as there was no corresponding temperature increase on-axis upstream in figure 6 (c). It can be concluded that the increased neutral gas heating is related to the increased power deposition via the increased radial ion flux adjacent to the powered electrode, as shown previously in figure 5 (d).

4.2 Influence of the ion power deposition fraction on neutral gas temperature

The ion power fraction, defined as the ratio between power deposited into Ar^+ and the total rf-power deposited, is shown with respect to applied voltage for a single frequency 600 V_{pp}, 13.56 MHz discharge in figure 7 (a) and with respect to phase offset for two dual-frequency 600 V_{pp} voltage waveforms, odd-even and odd-odd, in figures 7 (b) and (c), respectively.

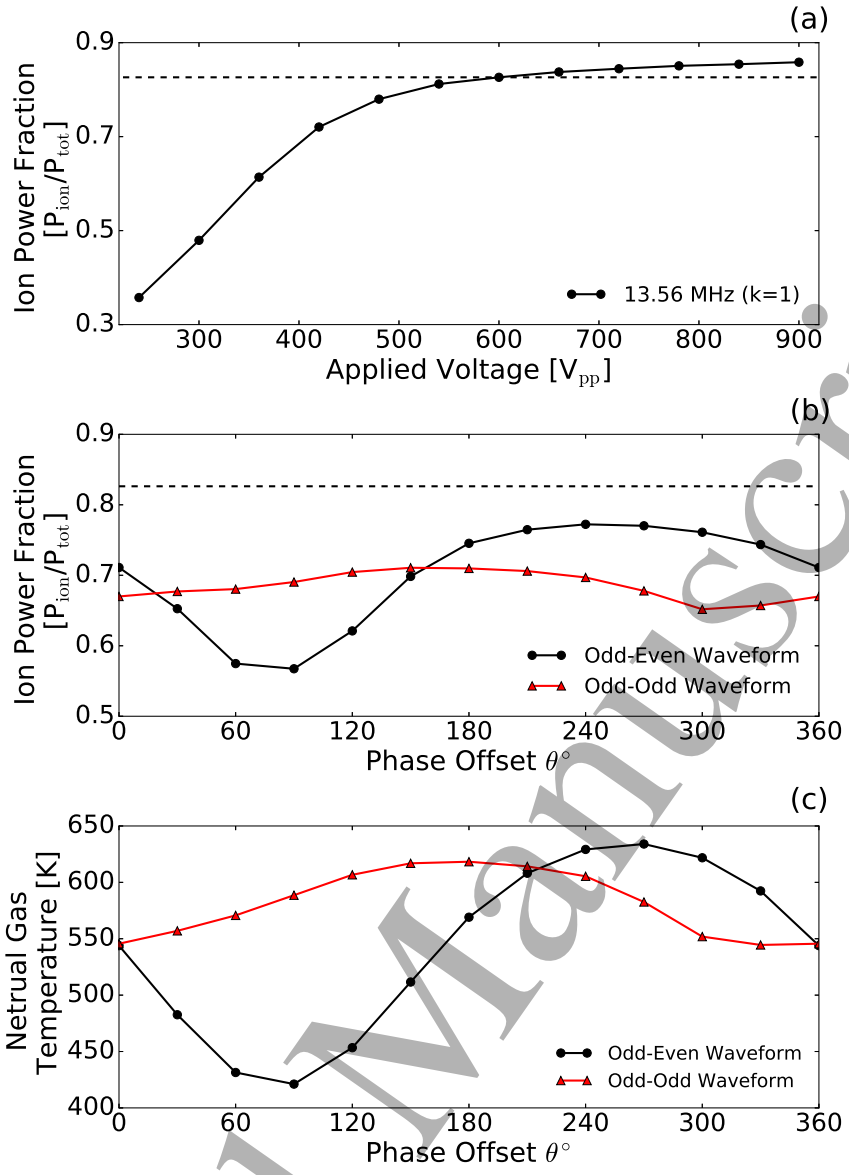

Figure 7: Ion power fraction for (a) a single frequency 13.56 MHz waveform with respect to applied voltage and (b) two dual-frequency voltage waveforms, odd-even and odd-odd respectively, and (c) the resulting neutral gas temperature on-axis at the powered electrode (R,Z = 0.0 mm, 21 mm), with respect to phase offset for the dual-frequency cases. The dashed lines on (a) and (b) represent the ion power fraction for a 600 V_{pp} single frequency 13.56 MHz, for ease of comparison. Plenum pressure 200 Pa (1.5 Torr), $\phi_0 = 600$ V.

In a single frequency 13.56 MHz discharge the ion power fraction increased with respect to the applied voltage as shown in figure 7 (a). This increase was greatest for lower voltages (240 - 600 V_{pp}) and began to plateau at $\approx$ 90% for voltages above 600 V_{pp}. The voltage range 240 - 600 V_{pp} approximately corresponds to α-mode operation, while voltages above 600 V_{pp} ($\phi_0 = 600$ V) correspond to γ-mode operation[16]. Note that although $\phi_0 = 600$ V is maintained for the dual-frequency waveforms, the resulting peak-to-peak voltage is typically slightly lower due to destructive interference between the two waveforms.

The variation in ion power fraction with phase offset in figure 7 (b) was largest for the odd-even voltage waveforms with a modulation of 20% between maximum and minimum compared with only a

6% modulation for the odd-odd voltage waveforms. Note that the reduction in the ion power fraction for the odd-even voltage waveforms was greatest at the most positive dc self-bias voltage ($\theta = 90°$) and similarly the highest ion power fraction occurred at the most negative dc self-bias voltage ($\theta = 270°$). Further, the up-moderated section of the ion power fraction ($180° \leq \theta \leq 300°$) is 'flatter' than the down-moderated section ($0° \leq \theta \leq 150°$). This is mirrored in the dc self-bias voltage shown previously in figure 5 (a).

The phase-averaged on-axis neutral gas temperature adjacent to the powered electrode (Z = 21 mm), shown in figure 7 (c) varied proportionally with the ion power fraction for both odd-odd and odd-even voltage waveforms. The maximum on-axis neutral gas temperature was modulated by 35% and 13% for the odd-even and odd-odd waveforms, respectively. This supports previous work suggesting ion-neutral charge exchange collisions as the primary heating mechanism[9,65].

Figure 8 shows the radial power deposition into Ar^+ ions and electrons adjacent to the powered electrode (Z = 21 mm) and the resulting neutral gas temperature with respect to phase offset for odd-even voltage waveforms. These waveforms were chosen as they had the largest effect on neutral gas temperature. The total deposited rf-power densities, electron P_e power densities and ion P_i power densities for each phase offset are axially integrated along the source tube length (24 mm). The electron and ion power densities are normalized to the maximum total rf-power density, occurring at $\theta = 270°$. The resulting normalized axially integrated electron P_e and ion P_i power densities are shown with respect to phase offset in figures 8 (a) and (b), respectively. The maximum on-axis neutral gas temperature with respect to phase offset is plotted for comparison in figure 8 (c), this is the same data as previously shown in figure 7 (c).

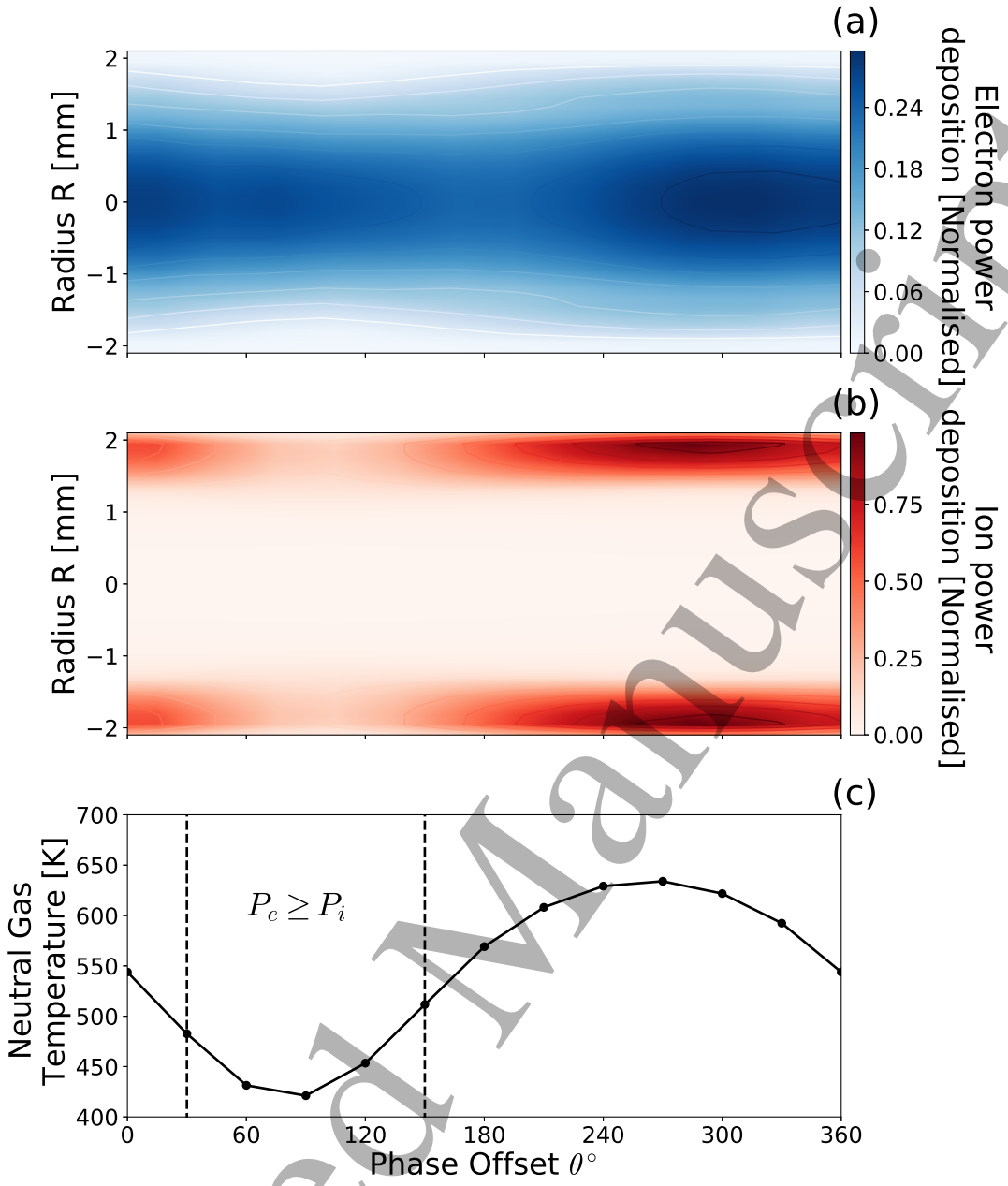

Figure 8: Phase-averaged axially integrated (a) electron and (b) ion rf-power densities, normalised to the radially integrated maximum total rf-power density at $\theta = 270°$ and (c) maximum on-axis neutral gas temperature, with respect to phase offset $0° \leq \theta \leq 360°$. Phases for which electron power depostion is greater than ion power deposition are between the black dashed lines in (c). Plenum pressure 200 Pa (1.5 Torr), $\phi_0 = 600$ V, odd-even dual-frequency voltage waveform.

Power is deposited into the electrons primarily on-axis, shown in figure 7 (a). Note that electron power deposition typically constitutes less than 25% of the total rf-power deposition, agreeing with figure 7. The increased electron power deposition between $240° \leq \theta \leq 360°$ correlates with the increased ionization due to secondary electrons observed in figure 5 (c). Further, a greater fraction of power is deposited closer to the wall for these phases, indicating an increased electron presence within the sheath (-1.0 mm $\leq$ R $\geq$ 1.0 mm). As such, the modulation in the electron power fraction is

primarily attributed to the variation in the secondary electron emission, and subsequent acceleration.

Figure 8 (b) presents the spatially-resolved modulation in the ion power fraction, previously discussed in figure 7 (b). Power is almost exclusively deposited into ions close to the radial walls, within the sheath (-1.0 mm $\leq$ R $\geq$ 1.0 mm). This indicates that power is primarily coupled into the ions by acceleration through the sheath potential, while electrons are primarily heated through collisions within the bulk and interactions with the sheath edge. Electron heating mechanisms are discussed in more detail in section 5.

As noted previously, the maximum on-axis neutral gas temperature in figure 8 (c) is directly proportional to the ion power fraction, with the lowest neutral gas temperatures between $30° \leq \theta \leq 150°$ where the electron power fraction is greater than the ion power fraction. Further, power is deposited into Ar^+ ions close to the dielectric wall adjacent to the powered electrode, coenciding with the regions of highest power deposition and neutral gas temperature in figures 6 (b) and (d), respectively. Finally, the variation in ion power fraction in figures 8 (b) and 7 (b) correlate with the variation in radial ion flux shown in figure 5 (d), indicating that the increased power is likely arising from the acceleration of more ions to higher velocities. It can therefore be concluded that the primary neutral gas heating mechanism is through ion-neutral charge-exchange collisions within the sheath, agreeing with previous work[9,66]. Additionally, as the radial ion flux is mediated by the dc self-bias voltage[16], tailored voltage waveforms provide a control mechanism for the neutral gas temperature.

5 Influence of the phase offset on electron and ion heating mechanisms

5.1 Electron heating dynamics

The phase offset between each dual-frequency waveform component has been shown to influence the ion power fraction and consequentially the neutral gas temperature. Further, the power deposited into electrons has been shown to exceed the ion power fraction for phase offsets between $30° \leq \theta \leq 150°$. To further investigate the effect of phase offset on the electron heating mechanisms the phase-resolved ionization rate resulting from electrons created in the gas phase, referred to here as 'bulk' ionization (not including secondary electrons) was analyzed in an odd-even dual-frequency driven discharge. Indirect effects from secondary electrons can be seen through electron-electron collisions and as secondary electrons 'relax' back into the bulk population when their energy drops below 3 eV[46]. The odd-even waveform was chosen as it had the largest effect on neutral gas temperature. Simulated PROES images in figures 9 (a) and (b) show the axially integrated Ar^+ 'bulk' ionization rate with respect the 27.12 MHz phase offset for $\theta = 90°$ and $\theta = 270°$, respectively. The associated phase-resolved voltage waveforms and dielectric surface potentials are shown in figures 9 (c) and (d), respectively.

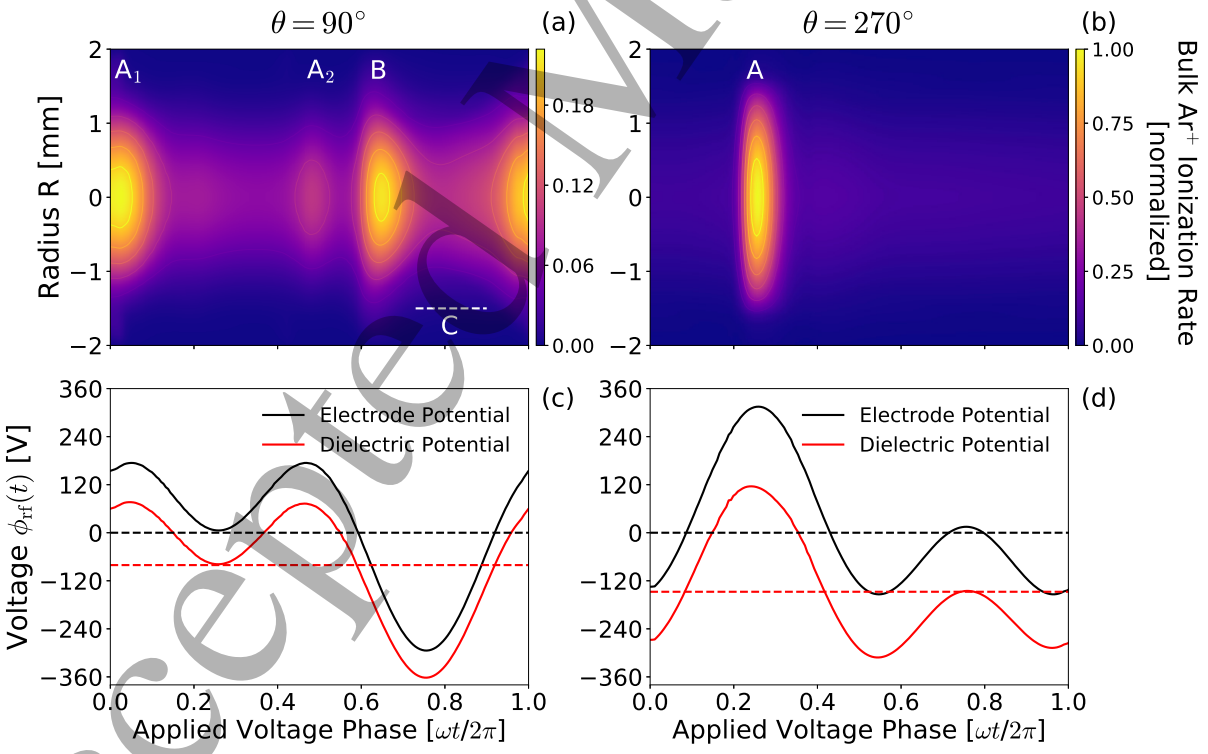

Figure 9: Phase-resolved axially integrated argon ionization rates with respect to rf-phase and associated applied voltage $\phi_{rf}(t)$, and dielectric potential adjacent to the powered electrode (Z = 21 mm) for an odd-even dual-frequency driven discharge with (a) (c) $\theta = 90°$ phase offset and (b) (d) $\theta = 270°$ phase offset. Dashed line in (a) denotes the period of increased ionization by secondary electrons. Plenum pressure 200 Pa (1.5 Torr), $\phi_0 = 600$ V, with an odd-even voltage waveform.

The phase-resolved ionization rate for the most positive dc self-bias voltage case, shown in figure 9 (a), exhibits three ionization structures (A_1, A_2 and B) and a varying on-axis 'background' ionization rate, highest during interval C. Two ionization structures, A_1 and A_2, are identified as the result of sheath collapse heating as they coincide with phases for which the applied voltage is most positive, $\omega t/2\pi = 0.05$ and $\omega t/2\pi = 0.5$. Note that the magnitude of the A_1 peak is greater in comparison to A_2 in figure 9 (a), this is likely the result of the increased production of secondary electrons as the dielectric potential becomes more negative during interval C between $0.7 \leq \omega t/2\pi \leq 0.9$. The increased electron flux into the plasma bulk during interval C results in a larger electron flux out of the bulk during sheath collapse at A_1, as compared to A_2, resulting in the increased ionization.

The ionization structure B, $\omega t/2\pi = 0.64$ in figure 9 (a), is the result of sheath expansion heating as it is aligned with the phase of most negative $\mathrm{d}V/\mathrm{d}t$[18]. A smaller ionization structure is also observed during the negative $\mathrm{d}V/\mathrm{d}t$ following peak A_1, however this is hard to distinguish from the background ionization.

The continuous background ionization in figure 9 (a) arises from argon atoms being ionized by ion-induced secondary electrons. As mentioned the effect of these secondary electrons is apparent in the 'bulk' ionization rate through relaxation into the bulk electron population. This background ionization possesses a time independent component as Ar^+ ions are accelerated by the phase-averaged negative dc self-bias voltage, shown in figure 9 (c) as the red dotted line. However as mentioned previously, the magnitude of the background ionization increases for phases where the applied voltage drops below this dc self-bias voltage, region C in figure 9 (a), leading to a higher radial ion flux and a higher secondary electron flux from the radial wall.

The phase-resolved ionization mechanisms were substantially altered when the phase offset was increased to $\theta = 270°$, as shown in figure 9 (b). Two changes are observed: only a single ionization peak exists at sheath collapse for $\omega t/2\pi = 0.23$, and the dc self-bias voltage becomes more negative, exhibited as a larger difference between the electrode potential and dielectric potential in figure 9 (d). Finally, the phase-averaged sheath width was observed to reduce between $\theta = 90°$ to $\theta = 270°$, previously shown in figures 6 (a) and (b), respectively.

The altered electron heating dynamics in figure 9 (b) can be explained in terms of the voltage waveform shape shown in figure 9 (d). Here, the $\theta = 270°$ voltage waveform exhibits positive amplitude asymmetry, i.e. the magnitude of the most positive amplitude $\omega t/2\pi \approx 0.2$ is greater than the magnitude of the most negative amplitude $\omega t/2\pi \approx 0.95$. Additionally, the reduction in the number of the ionization structures related to sheath collapse (peaks A, A_1 and A_2) indicates that the sheath is collapsed for a smaller fraction of the rf-cycle. This results in an accumulation of more negative charge within the

plasma bulk over the larger period of time between sheath collapses. To maintain quasineutrality the electron flux during sheath collapse must increase proportionally, leading to substantial electron heating during the shorter phase of sheath collapse.

5.2 Evolution of Ar^+ ionization rates with phase offset

In order to more clearly see the change in the temporal electron heating mechanisms with increasing phase offset, the simulated PROES images were spatially integrated and the resulting ionization profiles interpolated to produce figure 10. Here, the combined phase-resolved 'bulk' ionization rate and phase-averaged secondary ionization rate for each phase offset are plotted with respect to the applied voltage phase for an odd-even dual-frequency discharge.

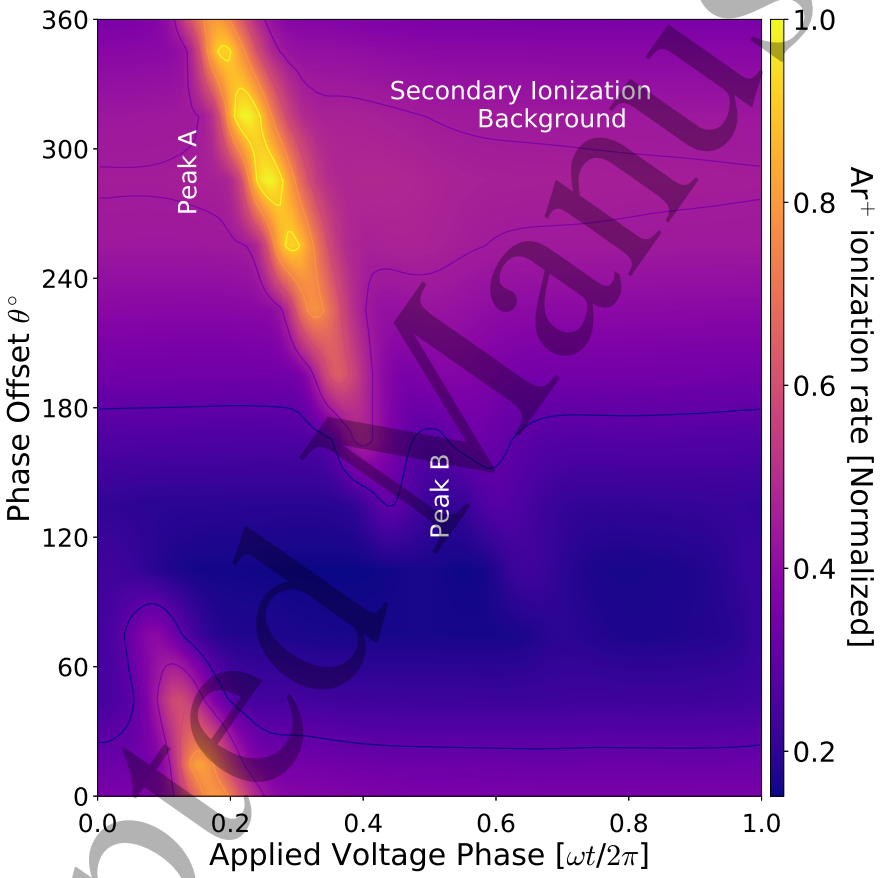

Figure 10: Spatially integrated Ar^+ ionization rate for odd-even dual-frequency waveforms with phase offsets in the range $0^\circ \leq \theta \leq 360^\circ$ with respect to rf-phase. Plenum pressure of 200 Pa (1.5 Torr), 13.56 MHz - 27.12 MHz, $\phi_0 = 600$ V.

Two ionization structures are visible in figure 10, peak A and peak B, corresponding to sheath collapse and sheath expansion, respectively. Increasing the phase offset results in the ionization structures occurring later in the rf phase-cycle for the resulting waveform. For each waveform, peak A characterizes the point in the rf phase-cycle where the applied voltage is reaching its most positive value, while peak B characterizes the point in the rf phase-cycle of greatest negative dV/dt, as previously shown in

figures 9 (a) and (b). Note that the 'background' ionization due to the secondary electron ionization is directly proportional to the dc self-bias voltage. The background ionization peaks between phase offsets of $270° \leq \theta \leq 300°$, corresponding to the most negative dc self-bias voltage and agreeing with the phase-averaged secondary ionization in figures 5 (a) and (c), respectively.

Varying the phase offset alters the magnitude and the phase for which the previously described electron heating mechanisms occur. A high degree of control over the electron heating mechanisms is achievable as evidenced by an approximately 70% reduction in the ionization associated with sheath collapse (peak A) for phase offsets $90° \leq \theta \leq 150°$. Similarly, sheath expansion can be made the dominant electron heating mechanism if a phase offset of $\theta \approx 100°$ is employed. Finally, as discussed previously, the phase-averaged sheath width can be regulated through the phase offset, which provides control over phase-averaged bulk plasma properties, such as radial ion flux and neutral gas temperatures.

5.3 Evolution of Ar($2p_1$) excitation rates with phase offset: Comparison with experiment

The simulated and measured Ar($2p_1$) phase-resolved excitation rates with respect to phase offset for an odd-even dual-frequency voltage waveform driven discharge are shown in figure 11 (a) and (b), respectively. As before, each PROES image has been spatially integrated for each phase offset and the resulting profiles combined to show the evolution of the temporally resolved heating mechanisms with respect to phase offset. Measurements were taken as previously described in section 3.

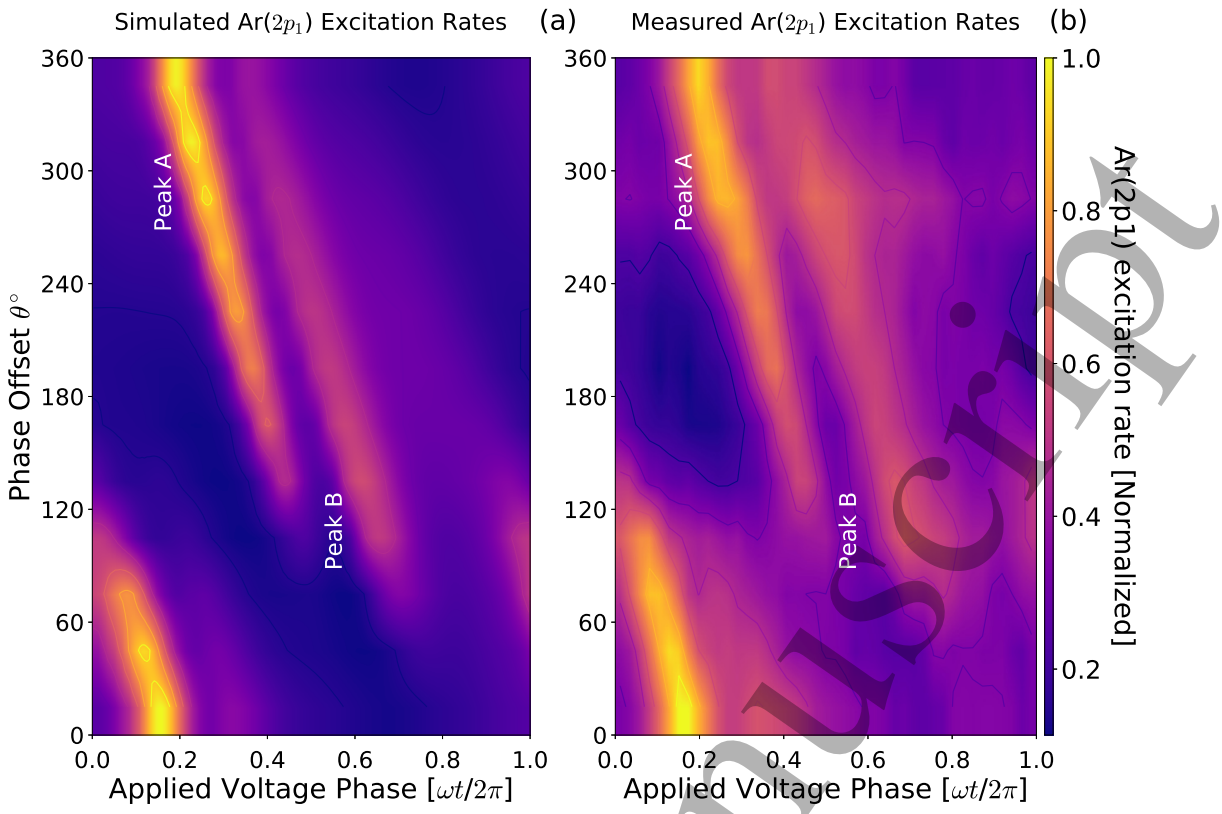

Figure 11: Spatially integrated (a) simulated and (b) measured Ar($2p_1$) excitation rates for odd-even dual-frequency waveforms with phase offsets in the range $0^\circ \leq \theta \leq 360^\circ$ with respect to rf phase. Simulation plenum pressure 200 Pa (1.5 Torr), experiment plenum pressure 207 Pa (1.55 Torr), simulation wall temperature determined with the two-step method as described in Ref 16, 13.56 MHz - 27.12 MHz, $\phi_0 = 600$ V.

The simulated Ar($2p_1$) excitation rates in figure 11 (a) show similarities to the ionization rates observed in figure 10. Sheath collapse heating (peak A) continues to represent the dominant heating mechanism, however sheath expansion heating (peak B) is now more easily distinguished from the background. Although the secondary electron background is visible for ionization rates in figure 10, it is not visible for excitation rates in figure 11 (a). This arises as secondary electrons preferentially undergo ionization interactions due to their high energy ($\approx$ 30 eV) relative to the Ar($2p_1$) excitation potential ($\approx$ 11 eV), resulting in a reduced excitation component from the secondary electron population.

The measured Ar($2p_1$) excitation rates in figure 11 (b) show a close agreement with the simulated rates in 11 (a). Excitation arising from both sheath collapse heating (peak A) and sheath expansion heating (peak B) are visible for the same range of rf phases over the same applied phase offsets. Additionally, the relative difference between the sheath collapse heating and sheath expansion heating is approximately the same for the simulated and measured PROES. Further, evidence of the control afforded by the dual-frequency phase offset is observed (albeit over a smaller phase offset range) in the measured PROES through a significant ($\approx 50\%$) reduction in the sheath collapse heating mechanism between $120^\circ \leq \theta \leq 150^\circ$.

However, it should be noted that the background excitation between phase offsets $240^\circ \leq \theta \leq 300^\circ$,

is higher than would be expected from the simulation. This range of phase offsets coincides with the phase offsets resulting in the most negative dc self-bias voltages and the peak secondary electron ionization background in figure 10. This could indicate that either the secondary electron induced $Ar(2p_1)$ excitation rates are underestimated in simulation or, noting that the electron excitation cross-section reduces with increasing energy, that the secondary electron energy is overestimated in simulation, resulting in a higher chance for excitation[43].

5.4 Ion Energy Distribution Functions

The Ar^+ ion energy distribution functions (IEDF) incident on the radial wall at region 2 (R,Z = 2.1 mm, 21 mm) are shown with respect to phase offset for odd-even and odd-odd dual-frequency voltage waveforms in figures 12 (a) and (b), respectively. The IEDFs are normalized such that the integral over all energies ϵ is equal to 1 and they have been angularly integrated for angles of incidence up to $\Theta = 45°$ symmetrically about the normal. Phase offsets that correspond to the most positive and negative dc self-bias voltages are shown in red and blue, respectively.

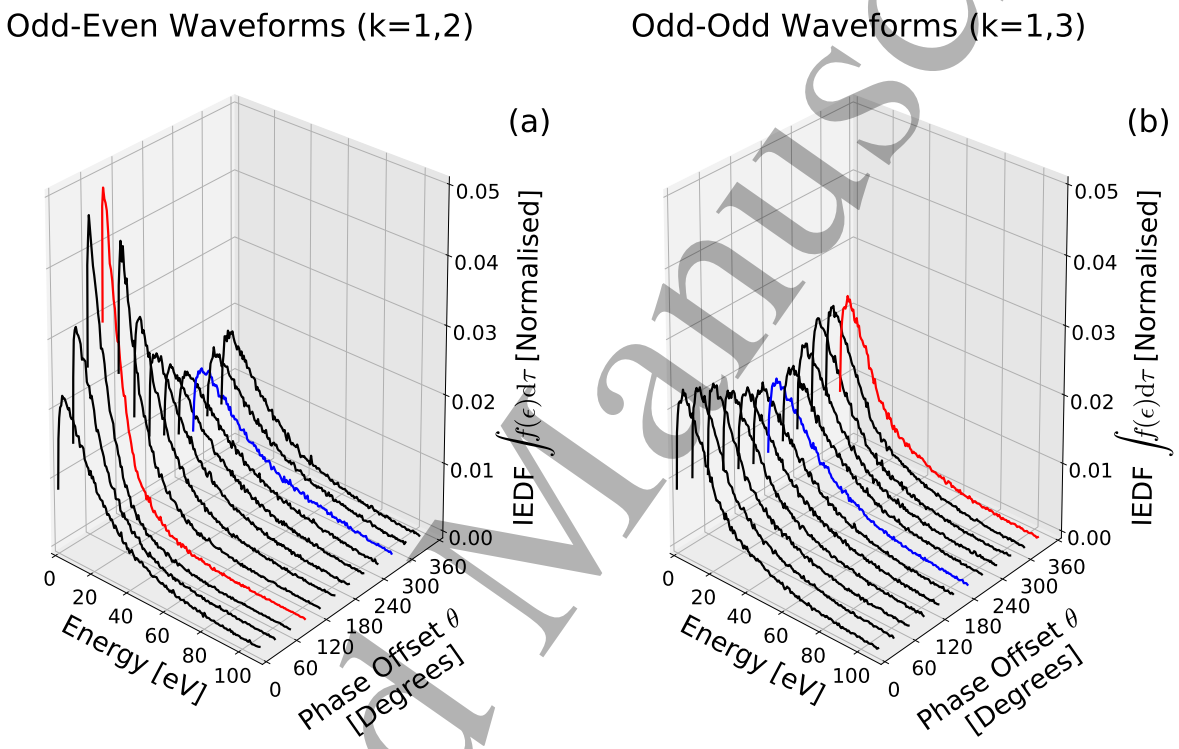

Figure 12: IEDF at the radial wall adjacent to the powered electrode (R,Z = 2.1 mm, 21 mm) for (a) odd-even and (b) odd-odd dual-frequency voltage waveforms. Phase offsets that correspond to the most positive and negative dc self-bias voltages are shown in red and blue, respectively. Plenum pressure of 200 Pa (1.5 Torr), $\phi_0 = 600$ V.

The IEDFs are all approximately Maxwellian in shape, with the majority of the ions impacting the radial wall at energies below 20 eV. Note also, that the dc self-bias voltage, and hence sheath voltage, is typically higher than 20 V (-148 V $\leq \eta \leq -80$ V), see figure 5. This disparity between the sheath voltage and ion energy at the radial wall surface arises as ions lose energy through ion-neutral charge-exchange collisions within the sheath, heating the neutral gas. It should be noted that the ion-neutral charge exchange cross-section reduces with increasing ion energy[43], and that excessively high modal ion energies could actually reduce the neutral gas heating efficiency. However, for sufficiently

collisional discharges, the reduction in the cross-section is secondary to the increased fraction of energy deposited into the ions, see figure 8, resulting in an increased overall gas heating.

The mean and modal values for the IEDFs presented in figures 12 (a) and (b) are shown with respect to phase offset in figures 13 (a) and (b), respectively. The electric field strength adjacent to the powered electrode at region 2 (R,Z = 2.1 mm, 21 mm) is shown in figure 13 (c)

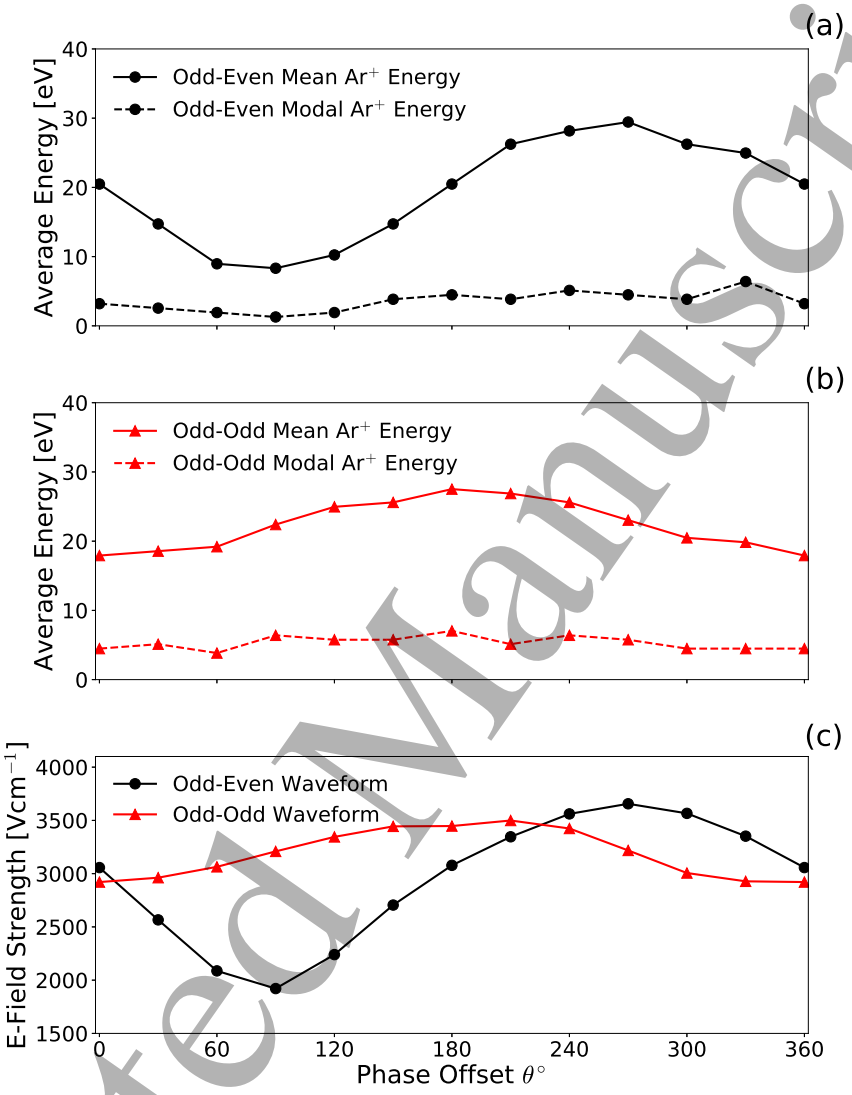

Figure 13: Mean and model values of the Ar^+ IEDF at the radial wall adjacent to the powered electrode (R,Z = 2.1 mm, 21 mm) with respect to phase offset for an (a) odd-even and (b) odd-odd dual-frequency voltage waveform discharge. Phase-averaged (c) maximum electric field strength for the same location with respect to phase offset. Plenum pressure of 200 Pa (1.5 Torr), ϕ_0 = 600 V.

The mean Ar^+ energy at the radial wall adjacent to the powered electrode increases from 8 eV to 29 eV for an odd-even discharge and 18 eV to 27 eV for an odd-odd discharge, shown in figures 13 (a) and (b), respectively. Odd-even waveforms provided a larger range of control over the IEDF, while odd-odd waveforms maintained a higher energy for the same operating voltage and phase offset. This trend was maintained for the modal Ar^+ energies, which varied between 1.3 eV to 6.4 eV, a factor of 4.92 modulation for the odd-even voltage waveforms and 3.8 eV to 7 eV, a factor of 1.84 modulation

for the odd-odd voltage waveforms.

The highest electric field strength adjacent to the powered electrode, shown in figure 13 (c), was found for an odd-even waveform with phase offset $\theta = 270°$, representing the waveform with the highest phase-averaged sheath width, see figure 6 (b). Ions gain their energy as they are accelerated through the sheath potential, therefore, increasing the fraction of the rf cycle for which the sheath is extended results in higher phase-averaged ion energies. The increased ion energies for $\theta = 270°$ reflect the change in the electron heating mechanisms shown in figure 9 (b), where the reduced frequency of sheath collapse heating indicates a higher phase-averaged sheath width.

A comparison between figures 9 (a) and 13 (c) indicates that voltage waveforms minimizing the fraction of rf-phase for which the powered electrode sheath is collapsed, i.e. most negative dc self-bias voltage, result in a higher phase-averaged electric field. Additionally, the increased Ar^+ ionization rates at the powered electrode due to the altered electron heating dynamics, see figure 10, result in an increased plasma density and an increased powered electrode sheath capacitance. This increased capacitance results in a larger powered electrode dielectric surface charge, compounding the reduction in the dc self-bias voltage shown in figure 5 (a). The same underlying mechanism, the phase-averaged sheath dynamics, are responsible for altering the electron heating mechanisms as for the modulation of the dc self-bias voltage. The degree of control offered by waveform voltage tailoring therefore depends upon the interdependent relationship between the sheath dynamics and the resulting ionization processes.

6 Conclusions

Control of the dc self-bias voltage in a dual-frequency driven hollow cathode radio-frequency (rf) electrothermal microthruster has been demonstrated through the use of experimentally validated 2D fluid/Monte-Carlo simulations performed using the Hybrid Plasma Equipment Model (HPEM). A comparison of measured phase resolved $Ar(2p_1)$ excitation rates to simulated rates showed a close agreement. Two types of dual-frequency voltage waveforms were investigated, comprising the combination of a 13.56 MHz fundamental waveform with either a 27.12 MHz or 40.68 MHz waveform applied with a variable phase offset. Varying the phase offset through $0° \leq \theta \leq 360°$ produced a dc self-bias voltage modulation of 11% V_{pp} and 3% V_{pp} of the maximum applied V_{pp} for the odd-even and odd-odd voltage waveforms, respectively. The magnitude of the dc self-bias voltage was found to correlate with the fraction of rf-power deposited into Ar^+ ions within the plasma. Through varying the phase offset in an odd-even waveform discharge the ion power fraction was varied from 57% to 77% of the total rf-power deposited, resulting in a 225% variation in the Ar^+ density, a 35% variation

in the on-axis neutral gas temperature and a factor of 5 variation in the modal ion energy adjacent to the powered electrode wall. The underlying mechanism is proposed to be a reduction in the fraction of the rf-cycle for which the sheath is collapsed and the resultant increase in the phase-averaged radial electric field strength and sheath capacitance. The application of dual-frequency waveforms to plasma sources provides the ability to selectively enhance specific heating mechanisms within the plasma by controlling the phase-resolved sheath dynamics. Such control allows for an optimization of electron, ion and neutral heating mechanisms and power deposition relevant to the desired source function, e.g. optimization of neutral gas heating mechanisms for spacecraft propulsion or enhancement of ionization rate and surface incident ion fluxes for industrial applications. Further work into exploring the effects of higher harmonic waveforms could allow for separate control of ion densities and energies in hollow cathode geometries.

7 Acknowledgements

The authors wish to thank Prof. M. J. Kushner for provision of the HPEM source code and ongoing fruitful discussions as well as Richard Armitage for technical support. The work presented herein was funded by the Engineering and Physical Sciences Research Council (EPSRC, EP/M508196/1).

8 References

[1] D. M. Goebel and I. Katz. *Fundamentals of Electric Propulsion*. Hokoken, NJ: Wiley, 2008.

[2] I. Levchenko, K. Bazaka, Y. Ding, Y. Raitses, S. Mazouffre, T. Henning, Peter J. Klar, S. Shinohara, J. Schein, L. Garrigues, M. Kim, D. Lev, F. Taccogna, R. W. Boswell, C. Charles, H. Koizumi, Y. Shen, C. Scharlemann, M. Keidar, and S. Xu. Space micropropulsion systems for Cubesats and small satellites: From proximate targets to furthermost frontiers. *Applied Physics Reviews*, 5(1), 2018. ISSN 19319401. doi:10.1063/1.5007734.

[3] D. Rafalskyi and A. Aanesland. Brief review on plasma propulsion with neutralizer-free systems. *Plasma Sources Science and Technology*, 25(4), 2016. ISSN 13616595. doi:10.1088/0963-0252/25/4/043001.

[4] I. Adamovich, S. D. Baalrud, A. Bogaerts, P. J. Bruggeman, M. Cappelli, V. Colombo, U. Czarnetzki, U. Ebert, J. G. Eden, P. Favia, D. B. Graves, S. Hamaguchi, G. Hieftje, M. Hori, I. D. Kaganovich, U. Kortshagen, M. J. Kushner, N. J. Mason, S. Mazouffre, S. Mededovic Thagard, H. R. Metelmann, A. Mizuno, E. Moreau, A. B. Murphy, B. A. Niemira, G. S. Oehrlein, Z. Lj Petrovic, L. C. Pitchford, Y. K. Pu, S. Rauf, O. Sakai, S. Samukawa, S. Starikovskaia, J. Tennyson, K. Terashima, M. M. Turner, M. C.M. Van De Sanden, and A. Vardelle. The 2017 Plasma Roadmap: Low temperature plasma science and technology. *Journal of Physics D: Applied Physics*, 50(32), 2017. ISSN 13616463. doi:10.1088/1361-6463/aa76f5.

[5] M. Keidar, T. Zhuang, A. Shashurin, G. Teel, D. Chiu, J. Lukas, S. Haque, and L. Brieda. Electric propul-

sion for small satellites. *Plasma Physics and Controlled Fusion*, 57(1), 2015. ISSN 13616587. doi:10.1088/0741-3335/57/1/014005.

[6] A. Poghosyan and A. Golkar. CubeSat evolution: Analyzing CubeSat capabilities for conducting science missions. *Progress in Aerospace Sciences*, 88(November 2016):59–83, 2017. ISSN 03760421. doi:10.1016/j.paerosci.2016.11.002.

[7] C. Charles and R. W. Boswell. Measurement and modelling of a radiofrequency micro-thruster. *Plasma Sources Science and Technology*, 21(2):022002, 2012. ISSN 0963-0252. doi:10.1088/0963-0252/21/2/022002.

[8] C. Charles, J. Dedrick, R. W. Boswell, D. O'Connell, and T. Gans. Nanosecond optical imaging spectroscopy of an electrothermal radiofrequency plasma thruster plume. *Applied Physics Letters*, 103(12):124103, 2013. ISSN 00036951. doi:10.1063/1.4821738.

[9] A. Greig, C. Charles, N. Paulin, and R. W. Boswell. Volume and surface propellant heating in an electrothermal radio-frequency plasma micro-thruster. *Applied Physics Letters*, 105(5):054102, 2014. ISSN 0003-6951. doi:10.1063/1.4892656.

[10] A. Greig, C. Charles, and R. W. Boswell. Simulation of main plasma parameters of a cylindrical asymmetric capacitively coupled plasma micro-thruster using computational fluid dynamics. *Frontiers in Physics*, 2(January): 1–9, 2015. ISSN 2296-424X. doi:10.3389/fphy.2014.00080.

[11] T. S. Ho, C. Charles, and R. W. Boswell. A Comprehensive Cold Gas Performance Study of the Pocket Rocket Radiofrequency Electrothermal Microthruster. *Frontiers in Physics*, 4(January):1–16, 2017. ISSN 2296-424X. doi:10.3389/fphy.2016.00055.

[12] T. S. Ho, C. Charles, and R. Boswell. Neutral gas heating and ion transport in a constricted plasma flow. *Physics of Plasmas*, 24(8):8–13, 2017. ISSN 10897674. doi:10.1063/1.4996014.

[13] T. S. Ho, C. Charles, and R. W. Boswell. Performance modelling of plasma microthruster nozzles in vacuum. *Journal of Applied Physics*, 123(17):173301, 2018. ISSN 0021-8979. doi:10.1063/1.5012765.

[14] C. Charles, R. Hawkins, and R. W. Boswell. Particle in cell simulation of a radiofrequency plasma jet expanding in vacuum. *Applied Physics Letters*, 106(9):093502, 2015. ISSN 0003-6951. doi:10.1063/1.4914109.

[15] C. Charles, W. Liang, L. Raymond, J. Rivas-Davila, and R. W. Boswell. Vacuum Testing of a Miniaturized Switch Mode Amplifier Powering an Electrothermal Plasma Micro-Thruster. *Frontiers in Physics*, 5(August):1–8, 2017. ISSN 2296-424X. doi:10.3389/fphy.2017.00036.

[16] S. J. Doyle, A. R. Gibson, J. Flatt, T. S. Ho, R. W. Boswell, C. Charles, P. Tian, M. J. Kushner, and J. Dedrick. Spatio-temporal plasma heating mechanisms in a radio-frequency electrothermal microthruster. *Plasma Sources Science and Technology*, 27:085011, 2018. doi:10.1088/1361-6595/aad79a.

[17] A. Greig, C. Charles, R. Hawkins, and R. Boswell. Direct measurement of neutral gas heating in a radio-frequency electrothermal plasma micro-thruster. *Applied Physics Letters*, 103(7):1–7, 2013. ISSN 00036951. doi:10.1063/1.4818657.

[18] P. Chabert and N. Braithwaite. *Physics of Radio-Frequency Plasmas*. Cambridge University Press, Cambridge, 3rd edition, 2014.

[19] B. Bruneau, T. Novikova, T. Lafleur, J.-P. Booth, and E. V. Johnson. Control and optimization of the slope asymmetry effect in tailored voltage waveforms for capacitively coupled plasmas. *Plasma Sources Science and Technology*, 24:015021, 2015. ISSN 0963-0252. doi:10.1088/0963-0252/24/1/015021.

[20] M. A. Lieberman and A. J. Lichtenberg. *Principles of Plasma Discharges and Materials Processing*. John Wiley & Sons, New Jersey, 2nd edition, 2005. ISBN 0-471-72001-1. doi:10.1017/CBO9781107415324.004.

[21] B. G. Heil, U. Czarnetzki, R. P. Brinkmann, and T. Mussenbrock. On the possibility of making a geometrically symmetric RF-CCP discharge electrically asymmetric. *Journal of Physics D: Applied Physics*, 41(16):165202, 2008. ISSN 0022-3727. doi:10.1088/0022-3727/41/16/165202.

[22] J. Schulze, E. Schüngel, Z. Donkó, and U. Czarnetzki. The electrical asymmetry effect in multi-frequency capacitively coupled radio frequency discharges. *Plasma Sources Science and Technology*, 20(1), 2011. ISSN 09630252. doi:10.1088/0963-0252/20/1/015017.

[23] B. Bruneau, T. Gans, D. O'Connell, A. Greb, E. V. Johnson, and J.-P. Booth. Strong Ionization Asymmetry in a Geometrically Symmetric Radio Frequency Capacitively Coupled Plasma Induced by Sawtooth Voltage Waveforms. *Physical Review Letters*, 114(12):125002, 2015. ISSN 0031-9007. doi:10.1103/PhysRevLett.114.125002.

[24] T. Lafleur. Tailored-waveform excitation of capacitively coupled plasmas and the electrical asymmetry effect. *Plasma Sources Science and Technology*, 25(1):013001, 2016. ISSN 0963-0252. doi:10.1088/0963-0252/25/1/013001.

[25] T. Lafleur, P. Chabert, M. M. Turner, and J.-P. Booth. Theory for the self-bias formation in capacitively coupled plasmas excited by arbitrary waveforms. *Plasma Sources Science and Technology*, 22(6):065013, 2013. ISSN 0963-0252. doi:10.1088/0963-0252/22/6/065013.

[26] T. Lafleur, P. Chabert, and J.-P. Booth. Secondary electron induced asymmetry in capacitively coupled plasmas. *Journal of Physics D: Applied Physics*, 46(13):135201, 2013. ISSN 0022-3727. doi:10.1088/0022-3727/46/13/135201.

[27] Ihor Korolov, Aranka Derzsi, and Julian Schulze. asymmetry effect in capacitively coupled plasmas The influence of the secondary electron induced asymmetry on the electrical asymmetry effect in capacitively coupled plasmas. 064102(2013):1–5, 2014. doi:10.1063/1.4817920.

[28] I. Korolov, A. Derzi, Z. Donkó, E. Schüngel, and J. Schulze. The influence of electron reflection / sticking coefficients at the electrodes on plasma parameters in particle-in-cell simulations of capacitive radio-frequency plasmas. *Plasma Sources Science and Technology*, 25:015024, 2016. doi:10.1088/0963-0252/25/1/015024.

[29] J. Schulze, Z. Donkó, D. Luggenhölscher, and U. Czarnetzki. Different modes of electron heating in dual-frequency capacitively coupled radio frequency discharges. *Plasma Sources Science and Technology*, 18:034011, 2009. ISSN 0963-0252. doi:10.1088/0963-0252/18/3/034011.

[30] S. J. Doyle, T. Lafleur, A. R. Gibson, P. Tian, M. J. Kushner, and J. Dedrick. Enhanced control of the ionization rate in radio-frequency plasmas with structured electrodes via tailored voltage waveforms. *Plasma Sources Science and Technology*, 26:125005, 2017. doi:10.1088/1361-6595/aa96e5.

[31] A. R. Gibson, A. Greb, W. G. Graham, and T. Gans. Tailoring the nonlinear frequency coupling between odd harmonics for the optimisation of charged particle dynamics in capacitively coupled oxygen plasmas. *Applied Physics Letters*, 106(5), 2015. ISSN 00036951. doi:10.1063/1.4907567.

[32] A. R. Gibson and T. Gans. Controlling plasma properties under differing degrees of electronegativity using odd harmonic dual frequency excitation. *Plasma Sources Science and Technology*, 26(11), 2017. ISSN 13616595. doi:10.1088/1361-6595/aa8dcd.

[33] S. Brandt, B. Berger, E. Schüngel, I. Korolov, A. Derzsi, B. Bruneau, E. Johnson, T. Lafleur, D. O'Connell, M. Koepke, T. Gans, J. P. Booth, Z. Donkó, and J. Schulze. Electron power absorption dynamics in capacitive radio frequency discharges driven by tailored voltage waveforms in CF4. *Plasma Sources Science and Technology*, 25(4):45015, 2016. ISSN 13616595. doi:10.1088/0963-0252/25/4/045015.

[34] Y. Zhang, A. Zafar, D. J. Coumou, S. C. Shannon, and M. J. Kushner. Control of ion energy distributions using phase shifting in multi-frequency capacitively coupled plasmas. *Journal of Applied Physics*, 117(23):1–15, 2015. ISSN 10897550. doi:10.1063/1.4922631.

[35] Y. Du and Y. Li. Plasma Density Distribution in Asymmetric Geometry Capacitive Coupled Plasma Discharge System. *World Academy of Science, Engineering and Technology*, 6(11):919–922, 2012.

[36] E. Schüngel, J. Schulze, Z. Donkó, and U. Czarnetzki. Power absorption in electrically asymmetric dual frequency capacitive radio frequency discharges. *Physics of Plasmas*, 18(1), 2011. ISSN 1070664X. doi:10.1063/1.3535542.

[37] J. Schulze, E. Schüngel, U. Czarnetzki, and Z. Donko. Optimization of the electrical asymmetry effect in dual-frequency capacitively coupled radio frequency discharges: Experiment, simulation, and model. *Journal of Applied Physics*, 106(6), 2009. ISSN 00218979. doi:10.1063/1.3223310.

[38] E. Schüngel, D. Eremin, J. Schulze, T. Mussenbrock, and U. Czarnetzki. The electrical asymmetry effect in geometrically asymmetric capacitive radio frequency plasmas. *Journal of Applied Physics*, 112(5), 2012. ISSN 00218979. doi:10.1063/1.4747914.

[39] J. Schulze, B. G. Heil, D. Luggenhölscher, R. P. Brinkmann, U. Czarnetzki, and D. Luggenh. Stochastic heating in asymmetric capacitively coupled RF discharges. *Journal of Physics D: Applied Physics*, 41(19):195212, 2008. ISSN 0022-3727. doi:10.1088/0022-3727/41/19/195212.

[40] J. Schulze, E. Schüngel, U. Czarnetzki, M. Gebhardt, R. P. Brinkmann, and T. Mussenbrock. Making a geometrically asymmetric capacitive rf discharge electrically symmetric. *Applied Physics Letters*, 98(3):7–10, 2011. ISSN 00036951. doi:10.1063/1.3544541.

[41] A. Derzsi, I. Korolov, E. Schüngel, Z. Donkó, and J. Schulze. Effects of fast atoms and energy-dependent secondary electron emission yields in PIC/MCC simulations of capacitively coupled plasmas. *Plasma Sources Science and Technology*, 24(3), 2015. ISSN 13616595. doi:10.1088/0963-0252/24/3/034002.

[42] K. H. Schoenbach, A. El-habachi, W. Shi, and M. Ciocca. High-pressure hollow cathode discharges. *Plasma Sources Science and Technology*, 6:468–477, 1997. doi:10.1088/0963-0252/6/4/003.

[43] A. V. Phelps and Z. Lj. Petrovic. Cold-cathode discharges and breakdown in argon: surface and gas phase production of secondary electrons. *Plasma Sources Science and Technology*, 8(3):R21–R44, 1999. ISSN 0963-0252. doi:10.1088/0963-0252/8/3/201.

[44] T. Lafleur and P. Chabert. Is collisionless heating in capacitively coupled plasmas really collisionless? *Plasma Sources Science and Technology*, 24(4), 2015. ISSN 13616595. doi:10.1088/0963-0252/24/4/044002.

[45] P. C. Boyle, A. R. Ellingboe, and M. M. Turner. Independent control of ion current and ion impact energy onto electrodes in dual frequency plasma devices. *Journal of Physics D: Applied Physics*, 37:697–701, 2004. ISSN 0022-3727. doi:10.1088/0022-3727/37/5/008.

[46] M. J. Kushner. Hybrid modelling of low temperature plasmas for fundamental investigations and equipment design. *Journal of Physics D: Applied Physics*, 42(19):194013, 2009. ISSN 0022-3727. doi:10.1088/0022-3727/42/19/194013.

[47] T Gans, Chun C Lin, V Schulz-von der Gathen, and H F Döbele. Determination of quenching coefficients in a hydrogen RF discharge by time-resolved. *Journal of Physics D: Applied Physics*, 34, 2001. doi:10.1088/0022-3727/34/8/101.

[48] T. Gans, D. O'Connell, V. Schulz-von der Gathen, and J. Waskoenig. The challenge of revealing and tailoring the dynamics of radio-frequency plasmas. *Plasma Sources Science and Technology*, 19(3):034010, 2010. ISSN 0963-0252. doi:10.1088/0963-0252/19/3/034010.

[49] J. Schulze, E. Schüngel, Z. Donkó, D. Luggenhölscher, and U. Czarnetzki. Phase resolved optical emission spectroscopy: a non-intrusive diagnostic to study electron dynamics in capacitive radio frequency discharges. *Journal of Physics D: Applied Physics*, 43(12):124016, 2010. ISSN 0022-3727. doi:10.1088/0022-3727/43/12/124016.

[50] P. Tian and M. J. Kushner. Controlling VUV photon fluxes in low-pressure inductively coupled plasmas. *Plasma Sources Science and Technology*, 24:34017, 2015. ISSN 0963-0252. doi:10.1088/0963-0252/24/3/034017.

[51] M. A. Furman and M. T. F. Pivi. Probabilistic model for the simulation of secondary electron emission. *Physical Review Special Topics - Accelerators and Beams*, 5(12):82–99, 2002. ISSN 10984402. doi:10.1103/PhysRevSTAB.5.124404.

[52] S.-H. Song and M. J. Kushner. Control of electron energy distributions and plasma characteristics of dual frequency, pulsed capacitively coupled plasmas sustained in Ar and Ar/CF4/O2. *Plasma Sources Science and Technology*, 21 (5):55028, 2012. ISSN 0734-2101. doi:10.1088/0963-0252/21/5/055028.

[53] M. Hayashi. Report No. IPPJ-AM-19. Technical report, Nagoya Institute of Technology, 1991.

[54] K. Tachibana. Excitation of the $1s_5$, $1s_4$, $1s_3$ and $1s_2$ levels of argon by low-energy electrons. *Physical Review A*, 34(2), 1986. doi:10.1103/PhysRevA.34.1007.

[55] D. Rapp and P. EnglanderGolden. Total Cross Sections for Ionization and Attachment in Gases by Electron Impact. I. Positive Ionization. *The Journal of Chemical Physics*, 43(5):1464–1479, 1965. ISSN 0021-9606. doi:10.1063/1.1696957.

[56] N. A. Dyatko, Y. Z. Ionikh, I. V. Kochetov, D. L. Marinov, A. V. Meshchanov, A. P. Napartovich, F. B. Petrov, and S. A. Starostin. Experimental and theoretical study of the transition between diffuse and contracted. *Journal of Physics D: Applied Physics*, 41:055204, 2008. doi:10.1088/0022-3727/41/5/055204.

[57] A. Bogaerts, R. G. V. Serikov, and V. V. Serikov. Calculation of gas heating in direct current argon glow discharges. *Journal of Applied Physics*, 87:8334, 1999. doi:10.1063/1.373545.

[58] H. W. Ellis, R. Y. Pai, E. W. McDaniel, E. A. Mason, and L. A. Viehland. Transport Properties of Gaseous Ions Over a Wide Energy Range. *Atomic Data and Nuclear Data Tables*, 17(3):177–210, 1976. doi:10.1016/0092-640X(76)90001-2.

[59] A. R. Gibson, M. Foucher, D. Marinov, P. Chabert, T. Gans, M. J. Kushner, and J.-P. Booth. The role of thermal energy accommodation and atomic recombination probabilities in low pressure oxygen plasmas. *Plasma Physics and Controlled Fusion*, 59:024004, 2017. doi:10.1088/1361-6587/59/2/024004.

[60] K. Niemi, S. Reuter, L. M. Graham, J. Waskoenig, N. Knake, V. Schulz-Von Der Gathen, and T. Gans. Diagnostic based modelling of radio-frequency driven atmospheric pressure plasmas. *Journal of Physics D: Applied Physics*, 43(12), 2010. ISSN 00223727. doi:10.1088/0022-3727/43/12/124006.

[61] A. Salaba and R. P. Brinkmann. Non-neutral/quasi-neutral plasma edge definition for discharge models: A numerical example for dual frequency hydrogen capacitively coupled plasmas. *Japanese Journal of Applied Physics, Part 1: Regular Papers and Short Notes and Review Papers*, 45(6 A):5203–5206, 2006. ISSN 00214922. doi:10.1143/JJAP.45.5203.

[62] N. Sadeghi, D. W. Setser, A. Francis, U. Czarnetzki, and H. F. Döbele. Quenching rate constants for reactions of Ar(4p[1/2]0, 4p[1/2]0, 4p[3/2]2, and 4p[5/2]2) atoms with 22 reagent gases. *Journal of Chemical Physics*, 115(7): 3144–3154, 2001. ISSN 00219606. doi:10.1063/1.1388037.

[63] R. A. Arakoni, J. J. Ewing, and M. J. Kushner. Microdischarges for use as microthrusters: modelling and scaling. *Journal of Physics D: Applied Physics*, 41(10):105208, 2008. ISSN 0022-3727. doi:10.1088/0022-3727/41/10/105208.

[64] J. Schulze, A. Derzsi, K. Dittmann, T. Hemke, J. Meichsner, and Z. Donkó. Ionization by drift and ambipolar electric fields in electronegative capacitive radio frequency plasmas. *Physical Review Letters*, 107(27):1–5, 2011. ISSN 00319007. doi:10.1103/PhysRevLett.107.275001.

[65] C. Charles, A. Bish, R. W. Boswell, J. Dedrick, A. Greig, R. Hawkins, and T. S. Ho. A Short Review of Experimental and Computational Diagnostics for Radiofrequency Plasma Micro-thrusters. *Plasma Chemistry and Plasma Processing*, 36(1):29–44, 2016. ISSN 02724324. doi:10.1007/s11090-015-9654-5.

[66] C. Charles, R. W. Boswell, and K. Takahashi. Investigation of radiofrequency plasma sources for space travel. *Plasma Physics and Controlled Fusion*, 54(12):124021, 2012. ISSN 0741-3335. doi:10.1088/0741-3335/54/12/124021.